Raman Studies of Surface Phonons in the Topological Insulators

Bi_2Se_3 and Bi_2Te_3

by

Ibrahim Boulares

A dissertation submitted in partial fulfillment
of the requirements for the degree of
Doctor of Philosophy
(Physics)
in the University of Michigan
2018

Doctoral Committee:

Professor Roberto D. Merlin, Chair
Associate Professor Hui Deng
Professor Mack Kira
Associate Professor Kai Sun
Professor Ctirad Uher

Ibrahim Boulares

ibrbrs@umich.edu

ORCID iD: 0000-0001-7252-4792

For my dad, mom and siblings.

ACKNOWLEDGMENTS

First and foremost, I would like to thank my advisor Prof. Roberto Merlin for all the support and guidance he provided throughout my PhD journey. His deep knowledge of condensed matter physics and intuition for experiments were pivotal on many occasions in my research. Roberto's ability to see the big picture and his persistent optimism—even in challenging times—have been inspirational. I have no doubt that such traits, which I hope to carry with me, will prove to be essential to my future success. Outside of the academic realm, Roberto deeply cared for his students' wellbeing and was always available for discussions, and for that, I am deeply grateful.

I would like to thank my committee members: Prof. Ctrad Uher for making available the necessary samples on which this study was conducted; Prof. Hui Deng for being my academic advisor in the early years of my PhD, and for helping me choose Roberto Merlin as my research advisor; Prof. Kai Sun for the insightful discussions on topological insulators; and Prof. Mack Kira for agreeing to be on my dissertation committee. I would also like to thank Prof. Manos Kioupakis and Guangsha Shi for their first-principles LDA calculations, which are presented in chapter IV.

Prior to joining Roberto's group, I had very little knowledge on how a laser operates. I would like to give thanks to Jingjing Li who took the time out of her very busy schedule as she was preparing for her defense to teach me about the fundamentals of Raman scattering and how to collect data. Special thanks to Steve Young, Meredith Henstridge, and Ilya Vugmeyster who introduced me to ultrafast experimental techniques and taught me how to carry out terahertz time domain measurements. Thanks to Steve for the insightful discussions on Raman scattering. Lastly but not least, I would like to thank Meredith Henstridge, Alex Toulouse, and Prashant Padmanabhan for the coffee breaks over which meaningful and—as often was the case—entertaining discussions took place.

Over the many years I spent in Ann Arbor, so many people have touched my life, and I would like to thank them all. I thank you very much for being great friends and for providing the love and comfort that kept me going.

My deep and sincere gratitude to my family who has been the greatest source of motivation and inspiration throughout my life. Thank you for the countless sacrifices that allowed me to take on new opportunities which otherwise would not have been possible.

Thank you!

TABLE OF CONTENTS

LIST OF FIGURES

ABSTRACT

Temperature- and wavelength- dependent Raman studies of the topological insulators Bi_2Se_3 and Bi_2Te_3 are presented. At low temperatures and in the *A* symmetry scattering channel, we observe additional weak modes which we ascribe to surface phonons. First-principles LDA calculations support such assignment in that they reveal surface phonons of *A* symmetry at frequencies which coincide with the extra lines observed experimentally. Moreover, wavelength-dependent measurements show that the surface phonon in Bi_2Se_3 displays an asymmetric Fano lineshape when the excitation frequency is near a resonance with a previously reported surface exciton [Kung *et al., Phys. Rev. Lett.* **119**, 136802 (2017)]. The lineshape asymmetry, which is a result of an interference between two scattering channels, reinforces our assignment of the extra peaks as due to surface modes and provides a measure of its coupling to surface electronic excitations.

CHAPTER I

Introduction

Since the first treatment of vibrational properties of free surfaces by Lord Rayleigh in 1887, surface phonons have seen an enormous increase in interest, particularly over the past 60 years [1]. This renewed interest is due to the development of experimental techniques which directly measure surface vibrational properties, such as electron energy loss spectroscopy and inelastic helium scattering. In addition, advancements made in supercomputers enabled theoretical predictions which in many cases are indispensable for the interpretation of experimental data. These developments paved the way to a surge of technological applications which rely on properties of surface vibrations [1]. The origin of surface phonons is due to the abrupt termination of the crystal. In other words, interfaces bring about phonon states which are split off from bulk phonon bands [1]. If the frequency of the surface phonon falls outside the range of the allowed bulk phonon frequencies, the mode is *localized* at the surface and is referred to as a "pure surface mode" [2]. However, if the frequency of the surface phonon overlaps in energy with a bulk band, the mode resonates with and decays into the bulk [2]. This mode is called a "surface resonance".

The work presented in this dissertation involves the study of surface phonons in bismuth selenide (Bi_2Se_3) and bismuth telluride (Bi_2Te_3). These materials have received significant attention from the science community in the last decade due to the new discovery of their peculiar

property as topological insulators (Tis). While insulating in the bulk, the surface of Tis are characterized with linearly dispersed and gapless metallic states which are protected against backscattering from time-reversal invariant defects and impurities [3,4,5,6,7,8,9]. Owing to their exotic surface properties, these materials are seen to provide a new possible avenue of achieving room-temperature superconductivity [10]. Therefore, studying processes which limit electron mobility at the surface is of great importance. Although the spin texture at the surface greatly suppresses spin scattering events [11,12], scattering involving other terms, such as electron-phonon coupling, is still possible and can significantly shorten the life time of these surface states [13]. Hence, identifying surface phonons and understanding their relevance to the topological states is crucial to characterizing the surface conductivity of these materials.

Raman spectroscopy proved to be a convenient and powerful tool in distinguishing surface excitations in TIs due the different characteristics of their surface and bulk electronic states. In resonant Raman scattering, when the energy of the incident and/or scattered light is near an interband transition or an exciton, Raman scattering cross-sections and, thus, intensities are largely enhanced. Consequently, by tuning the excitation energy to a known surface electronic transition, one can expect an enhancement in the scattering of surface collective excitations. A prior knowledge of the surface electronic states is, therefore, necessary. Luckily, since the discovery of the topological properties of Bi_2Se_3 and Bi_2Te_3, their surface electronic bands have been well characterized. For example, angle-resolved photoemission measurements (ARPES) in Bi_2Se_3 show two, occupied and unoccupied, Dirac surface states separated by ≈ 1.8 eV [14], so that in *n*-type samples, photons of ≈ 1.5 eV drive a direct transition from the low energy bulk conduction band into the unoccupied Dirac surface states [15]. Several Raman scattering studies exploited these properties in studying elementary excitations at the surface [16,17,18,19]. A Raman scattering

work on thin-film Bi_2Se_3, for instance, reveals an asymmetric Fano-shape-like peak, which was ascribed to an in-plane phonon mode, and its presence was attributed to a resonance enhancement when the incident photons have an energy of ≈ 1.5 eV [16]. Another Raman work reports on the observation of a surface chiral spin mode, which strongly resonates when the energy of the incoming photons are tuned to the transition between the two sets of Dirac cones [19].

In this dissertation, we employ wavelength- and temperature-dependent Raman measurements on the topological insulators Bi_2Se_3 and Bi_2Te_3 to provide new insights into the nature of their surface atomic vibrations and their relevance to the topological surface states. Prior to this work, the search for surface phonons in Bi_2Se_3 and Bi_2Te_3 produced controversial and sometimes contradictory results. For example, an electron energy loss scattering work in Bi_2Se_3 reported a peak at ~ 160 cm^{-1}, which was assigned to a surface phonon [20]. On the other hand, a Raman scattering work in single crystal Bi_2Se_3 also reported a peak at the same frequency, but was assigned to a bulk infrared mode [21]. Similar contradictory results and assignments were also reported on Bi_2Te_3 [22,23,24,25,26,27,28,29,30,31]. In chapter IV, we resolve this controversy. We show that extra modes in Bi_2Se_3 and Bi_2Te_3, which were previously assigned to infrared bulk modes, are instead localized surface phonons. First-principles local density approximations presented at the end of the chapter supports our contention. Moreover, and according to the calculations, the surface modes are quite insensitive to spin-orbit coupling, indicating that their occurrence is unrelated to the topological properties of these materials.

In chapter V we present low-temperature resonant Raman scattering data in which we observe the surface mode displaying an asymmetric Fano-profile when the excitation frequency is near resonance with a previously reported surface exciton [19]. The lineshape asymmetry, resulting from interference between two scattering channels, reinforces our assignment of the extra

lines as due to surface modes and provides a measure of its coupling to surface electronic excitations. Chapter II and III are devoted to the theoretical background of Raman scattering and the experimental methods carried out in this work, respectively.

References

[1] R.F. Wallis, Surf. Sci. 299-300, 612 (1994).

[2] G. Benedek and L. Miglio, Surface Phonons, ed. By W. Kress and F.W.de Wette (Springer-Verlag Berlin Heidelberg, 1981).

[3] L. Fu, C. L. Kane, and E. J. Mele, Phys. Rev. Lett. 98, 106803 (2007).

[4] H. Zhang, C.-X. Liu, X.-L. Qi, X. Dai, Z. Fang, and S.-C. Zhang, Nat. Phys. 5, 438 (2009).

[5] Y. L. Chen et al., Science 325, 178 (2009).

[6] Y. Xia et al., Nat. Phys. 5, 398 (2009).

[7] X.-L. Qi and S.-C. Zhang, Rev. Mod. Phys. 83, 1057 (2011).

[8] D. Hsieh et al., Science 323, 919 (2009).

[9] D. Hsieh et al., Nature (London) 460, 1101 (2009).

[10] X.-L. Qi & S.-C. Zhang, Rev. Mod. Phys. 83, 1057–1110 (2011).

[11] P. Roushan, J. Seo, C. V. Parker, Y. S. Hor, D. Hsieh, D. Qian, A. Richardella, M. Z. Hasan, R. J. Cava, and A. Yazdani, Nature (London) 460, 1106 (2009).

[12] T. Zhang et al., Phys. Rev. Lett. 103, 266803 (2009).

[13] N. P. Butch, K. Kirshenbaum, P. Syers, A. B. Sushkov, G. S. Jenkins, H. D. Drew, and J. Paglione, Phys. Rev. B 81, 241301 (2010).

[14] D. Niesner, Th. Fauster, S. V. Eremeev, T. V. Menshchikova, Yu. M. Koroteev, A. P. Protogenov, E. V. Chulkov, O. E. Tereshchenko, K. A. Kokh, O. Alekperov, A. Nadjfov, and N. Mamedov, Phys. Rev. B 86, 205403 (2012).

[15] J. A. Sobota, S.-L. Yang, A. F. Kemper, J. J. Lee, F. T. Schmitt, W. Li, R. G. Moore, J. G. Analytis, I. R. Fisher, P. S. Kirchmann, T. P. Devereaux, and Z,-X. Shen, Phys. Rev. Lett. 111. 136802 (2013).

[16] Y. D. Glinka, S. Babkiray, T. A. Johnson, and D. Lederman, J. Phys. Condens. Matter 27, 052203 (2015).

[17] Y. D. Glinka, S. Babkiray, and D. Lederman, J. Appl. Phys. 118, 135713 (2015).

[18] H. -H. Kung, M. Salehi, I. Boulares, A. F. Kemper, N. Koirala, M. Brahlek, P. Lošťák, C. Uher, R. Merlin, X. Wang, S.-W. Cheong, S. Oh, and G. Blumberg, Phys. Rev. B 95, 245406 (2017).

[19] H.-H. Kung, S. Maiti, X. Wang, S.-W. Cheong, D. L. Maslov and G. Blumberg, Phys. Rev. Lett. 119, 136802 (2017).

[20] A. Kogar, S. Vig, A. Thaler, M. H. Wong, Y. Xiao, D. Reig-i-Plessis, G. Y. Cho, T. Valla, Z. Pan, J. Schneeloch, R. Zhong, G. D. Gu, T. L. Hughes, G. J. MacDougall, T.-C. Chiang, and P. Abbamonte, Phys. Rev. Lett. 115, 257402 (2015).

[21] V. Gnezdilov, Y. G. Pashkevich, H. Berger, E. Pomjakushina, K. Conder, and P. Lemmens, Phys. Rev. B 84, 195118 (2011).

[22] K. M. F. Shahil, M. Z. Hossain, D. Teweldebrhan, and A. A. Balandin, Appl. Phys. Lett. 96, 153103 (2010).

[23] L. Ren, X. Qi, Y. Liu, G. Hao, Z. Huang, X. Zou, L. Yang, J. Li, and J. Zhong, J. Mater. Chem. 22, 4921 (2012).

[24] R. He, Z. Wang, R. L. J. Qiu, C. Delaney, B. Beck, T. E. Kidd, C. C. Chancey, and X. P. A. Gao, Nanotechnology. 23, 455703 (2012).

[25] S. M. Souza, D. M. Trichês, C. M. Poffo, J. C. de Lima, T. A. Grandi, and R. S. de Biasi, J. Appl. Phys. 109, 013512 (2011).

[26] Y. Liang, W. Wang, B. Zeng, G. Zhang, Y. Song, X. Zhang, J. Huang, J. Li, and T. Li, Solid State Commun. 151, 704 (2011).

[27] V. Goyal, D. Teweldebrhan, and A. A. Balandin, Appl. Phys. Lett. 97, 133117 (2010).

[28] M. Eddrief, P. Atkinson, V. Etgens, and B. Jusserand, Nanotechnology 25, 245701 (2010).

[29] S. Y. F. Zhao, C. Beekman, L. J. Sandilands, J. E. J. Bashucky, D. Kwok, N. Lee, A. D. LaForge, S. W. Cheong, and K. S. Burch, Appl. Phys. Lett. 98, 14911 (2011).

[30] C. Wang, X. Zhu, L. Nilsson, J. Wen, G. Wang, X. Shan, Q. Zhang, S. Zhang, J. Jia, and Q. Xue, Nano Res. 6, 688 (2013).

[31] H. -H. Kung, M. Salehi, I. Boulares, A. F. Kemper, N. Koirala, M. Brahlek, P. Lošťák, C. Uher, R. Merlin, X. Wang, S.-W. Cheong, S. Oh, and G. Blumberg, Phys. Rev. B 95, 245406 (2017).

CHAPTER II

General Theory of Raman Scattering by Optical Phonons

The theoretical and experimental description of phonon dynamics in crystals provide a wide range of information on a material's properties. Thermal, electronic, structural, and optical properties and more are dependent on the underlying phonon dynamics of a given material. For example, the interaction of light with insulators and semiconductors in the far-infrared region is dominated by phonons. Therefore, infrared transmission and reflection measurements are powerful tools for characterizing these vibrations. Other characterization methods of these collective excitations are inelastic x-ray, neutron, Brillouin, helium and Raman scattering. This work focuses on the interaction of light with atomic vibrations, and such interactions are studied by means of Raman spectroscopy. Raman spectroscopy is one of the main and convenient characterization methods used to obtain phonon vibrational frequencies at the zone center of or throughout the Brillouin zone for first- or higher- order scattering, respectively [1]. In addition, resonant Raman scattering, that is, the frequency dependence of the cross-section, also provides valuable information on interband optical excitations in crystals.

This chapter is devoted to the theoretical background of lattice vibrations and their interactions with light, with an emphasis on first-order interactions of visible and infrared light with optical phonons in non-polar materials. Section 2.1 provides a brief review of lattice dynamics, starting

from the classical formalism of normal modes before extending this formalism to the quantum picture of phonons. The well-known case of a one dimensional diatomic chain with nearest-neighbor interactions is discussed thereafter [2]. In Sections 2.2 and 2.3, the kinematics of inelastic light scattering by collective excitations is addressed along with a description of the experimentally measureable cross section in the macroscopic and microscopic picture. Section 2.4 is devoted to a review of key concepts of Raman scattering by long-wavelength lattice vibrations. The section concludes with a brief discussion on resonant Raman scattering and its implications. Finally, in section 2.5, a quick review of the theory of Fano-interference will be given.

1. Lattice Vibrations

Consider the total energy (Hamiltonian) of the atoms in a crystal. Suppose the s^{th} atom in the $\boldsymbol{l}^{th}$ unit cell with a mass of M_s has a displacement vector of $\boldsymbol{u_{sl}}$ from its equilibrium position and the total potential energy of the crystal is U. The total classical energy of all atoms in the crystal is expressed by

$$H_{total} = \sum_{sl} \frac{1}{2} M_s |\dot{\boldsymbol{u}}_{\boldsymbol{sl}}|^2 + U. \qquad (2.\ 1)$$

When all $\boldsymbol{u_{sl}} = 0$, the system is in equilibrium so that the potential energy is at a minima $U(\boldsymbol{u_{sl}} = 0) = U_0$. Suppose further that the displacements of the atoms are small enough that they result in small perturbations in the crystal's potential energy. Therefore, U can be approximated by a series expansion in terms of the Cartesian components $u_{\boldsymbol{sl}}^{j}$ as follows

$$U = U_0 + \sum_{slj} u_{\boldsymbol{sl}}^{j} \left[\frac{\partial U}{\partial u_{sl}^{j}}\right]_0 + \frac{1}{2} \sum_{ss'll'jj'} u_{\boldsymbol{sl}}^{j} u_{\boldsymbol{s'l'}}^{j'} \left[\frac{\partial^2 U}{\partial u_{sl}^{j} \partial u_{s'l'}^{j'}}\right]_0 + \cdots. \qquad (2.\ 2)$$

The first term is the potential energy of the crystal at equilibrium, which is a constant and therefore unimportant in deriving the equations of motion. The second term vanishes due to the assumption that the system is in equilibrium. Thus, the leading term in U is the third one, which contains the second derivative of U with respect to u_{sl}^{j}. Higher-order terms, which will not be considered, are responsible for the anharmonic behavior of the lattice vibrations [2]. The equations of motion are therefore [3]

$$M_s \ddot{\boldsymbol{u}}_{sl} = -\sum_{s'l'} \boldsymbol{G}_{sl,s'l'} \cdot \boldsymbol{u}_{s'l'}, \qquad \text{where } G_{sl,s'l'}^{jj'} = \left[\frac{\partial^2 U}{\partial u_{sl}^{j} \partial u_{s'l'}^{j'}}\right]_0. \qquad (2.\ 3)$$

Note that $\boldsymbol{G}_{sl,s'l'}$ is a second-rank tensor. Eq.2. 3 is an expression of the force experienced by the s^{th} atom in the unit cell $\boldsymbol{l}$ due to the displacement of each of the s'^{th} atoms in the $\boldsymbol{l}'^{\text{th}}$ cell. Since the forces experienced by the atoms depend only on the relative distance between them ($\boldsymbol{h} = \boldsymbol{l}' - \boldsymbol{l}$), Eq.2. 3 can be rewritten as

$$M_s \ddot{\boldsymbol{u}}_{sl} = -\sum_{s'\boldsymbol{h}} \boldsymbol{G}_{ss'}(h) \cdot \boldsymbol{u}_{s',\boldsymbol{l}+\boldsymbol{h}}. \qquad (2.\ 4)$$

Bloch's theorem states that, for a periodic potential, there is a wave vector $\boldsymbol{q}$ such that the displacement of an atom s in the unit cell l is related to the displacement of the atom at the origin as $\boldsymbol{u}_{sl}(t) = e^{i\boldsymbol{q}\cdot\boldsymbol{h}}\boldsymbol{u}_{s,0}(t)$. Therefore, it is sufficient to know the displacements of the atoms in one unit cell. Using this property in Eq.2. 4, we obtain

$$M_s \ddot{\boldsymbol{u}}_{s,0} = -\sum_{s'}\left[\sum_{\boldsymbol{h}} \boldsymbol{G}_{ss'}(h) e^{i\boldsymbol{q}\cdot\boldsymbol{h}}\right] \cdot \boldsymbol{u}_{s,0}. \qquad (2.\ 5)$$

Note that the number of equations of motion in Eq.2. 5 are reduced to three times the number of atoms per unit cell ($3n$). Now, assuming the solution has an oscillatory behavior in time with frequency ω_i, Eq.2. 5 becomes

$$\left[\sum_{s'}\left[\sum_{\boldsymbol{h}} \boldsymbol{G}_{\boldsymbol{ss'}}(\boldsymbol{h})e^{i\boldsymbol{q}\cdot\boldsymbol{h}}\right] - \omega_i^2 M_s \boldsymbol{I}\right]\cdot \boldsymbol{u}_{s,\boldsymbol{q}} = 0, \qquad (2.\ 6)$$

where $\boldsymbol{u}_{s,0}$ is replaced with $\boldsymbol{u}_{s,\boldsymbol{q}}$ to account for solutions with different values of $\boldsymbol{q}$. The determinant in the eigenvalue equation Eq.2. 6 must be zero for any non-trivial solutions. Therefore, for each value of the wavevector $\boldsymbol{q}$, there must be $3n$ solutions (or modes) to ω_i, where $\boldsymbol{q}$'s allowed values are the number of cells N in the crystal. In other words, there are $3n$ vibrational modes with frequencies ω_i ($i = 1,2,\ldots,3n$) that may vary in the reciprocal lattice space (Brillouin zones) as a function of $\boldsymbol{q}$. Three of these modes are acoustic in that $\omega_i(\boldsymbol{q}) = 0$ when $\boldsymbol{q} = 0$ [3].

It is possible to arrive at a simpler and more intuitive result for the atomic displacements if we transform to a new set of generalized coordinates known as normal coordinates [3]. This is obtained by diagonalizing the matrix in Eq.2. 6 through the use of eigenvector solutions. The Hamiltonian of the system in its normal coordinates takes the following simple form

$$H_{total} = U_0 + \sum_{i,\boldsymbol{q}} \frac{M}{2}\left|\dot{\boldsymbol{\xi}}_i(\boldsymbol{q})\right|^2 + \frac{1}{2}\sum_{i,\boldsymbol{q}} \omega_i(\boldsymbol{q})^2 |\boldsymbol{\xi}_i(\boldsymbol{q})|^2\,, \qquad (2.\ 7)$$

where M is the mass of the crystal, $\boldsymbol{\xi}_i$ is the normal coordinate and i is the branch index. It is now easy to develop the quantum mechanical formalism for lattice vibrations [4]. We first define the creation $b_{\boldsymbol{q}}^{+}$ and annihilation $b_{\boldsymbol{q}}^{-}$ operators as

$$b_{i\boldsymbol{q}}^{-} = \frac{\sqrt{M\omega_i}}{2\hbar}\boldsymbol{\xi}_i + i\sqrt{\frac{1}{2\hbar M\omega_i(\boldsymbol{q})}}\,\boldsymbol{p}_i(\boldsymbol{q}) \qquad (2.\ 8.a)$$

$$b_{i\boldsymbol{q}}^{+} = \frac{\sqrt{M\omega_i}}{2\hbar}\boldsymbol{\xi}_i - i\sqrt{\frac{1}{2\hbar M\omega_i(\boldsymbol{q})}}\boldsymbol{p}_i(\boldsymbol{q}), \qquad (2.\ 8.b)$$

where $\boldsymbol{p}_i(\boldsymbol{q}) = \frac{\dot{\xi}_i(\boldsymbol{q})}{2M}$. By substituting Eq.2. 8.a and Eq.2. 8.b in H_{total}, we arrive at

$$H_{total} = U_0 + \sum_{i,\boldsymbol{q}} \hbar\omega_i (b_{i\boldsymbol{q}}^{+} b_{i\boldsymbol{q}}^{-} + \frac{1}{2}). \qquad (2.\ 9)$$

This is the sum of the quantum energy $\hbar\omega_i$ of each mode in branch *i* with wavevector $\boldsymbol{q}$ multiplied by its population ($b_{i\boldsymbol{q}}^{+} b_{i\boldsymbol{q}}^{-}$) plus ½, where the factor ½ accounts for the zero-point motion energy. Each quantum of energy is called a phonon. For a full description of the quantum mechanical formalism of lattice vibrations see Peierls [5].

It is worth looking into a simple model to understand the physical properties of lattice waves. Consider a one-dimensional diatomic linear chain of atoms equally distant from each other and with the same spring constant α between adjacent atoms [2]. Consider also that two different

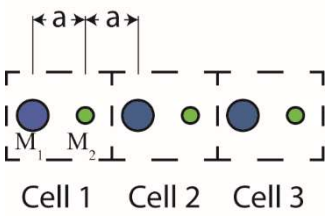

Figure 2.1: A schematic of a diatomic linear chain of masses M_1 and M_2 separated by a distance a when in equilibrium.

masses M_1 and M_2 are placed alternatively as shown in Fig.2.1. Following the previous procedure and considering only nearest-neighbor forces, the equations of motion in Eq.2. 5 reduce to

$$M_1\ddot{u}_1 = -2\alpha\, u_1 + 2\alpha\, cos(qa)\cdot u_2 \qquad (2.\ 10.a)$$

$$M_2\, \ddot{u}_2 = -2\alpha\, u_2 + 2\alpha\, \cos(qa)\cdot\ u_1, \qquad (2.\ 10.b)$$

where u_1 and u_2 are the atomic displacements of masses M_1 and M_2, respectively. The determinant in Eq.2. 6 for this case is

$$\begin{vmatrix} 2\alpha - M_1\nu^2 & -2\alpha\, cos(qa) \\ -2\alpha\, cos(qa) & 2\alpha - M_2\nu^2 \end{vmatrix} = 0, \qquad (2.\ 11)$$

which gives the following solutions for ω_i

$$\omega_{\pm}^2 = \alpha\left(\frac{1}{M_1}+\frac{1}{M_2}\right) \pm \alpha\sqrt{\left[\left(\frac{1}{M_1}+\frac{1}{M_2}\right)^2 - \frac{4\,sin^2(qa)}{M_1M_2}\right]} \qquad (2.\ 12)$$

Since $\omega_{\pm}$ is periodic with respect to q, all N solutions of $\omega_{\pm}$ are given when $\frac{-\pi}{2a} < q \leq \frac{\pi}{2a}$ (the Brillouin zone). Imposing periodic boundary conditions on Eq.2. 12 implies that $q = \frac{2\pi}{a}\frac{f}{N}$ where f is an integer spanning the values $\frac{-N}{2} < f \leq \frac{N}{2}$.

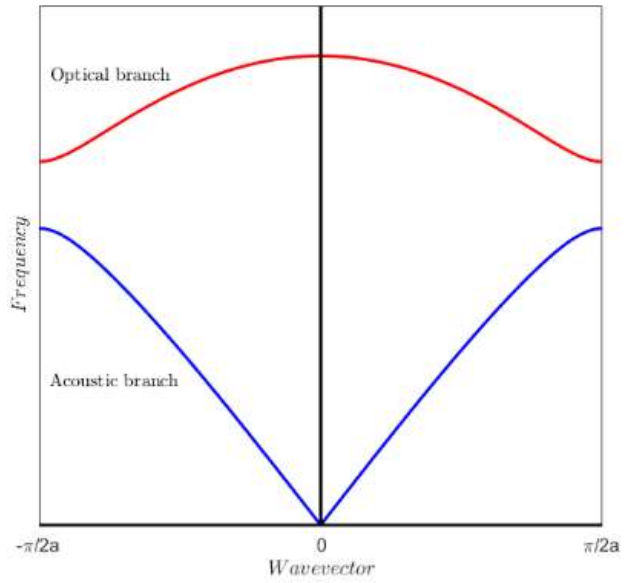

Figure 2.2: Phonon dispersion curve of a one-dimensional diatomic linear chain of masses M_1 and M_2.

The number of solutions to ω_i, in this case, is the number of atoms per unit cell (2) times the number of degrees of freedom per atom (1), in agreement with our previous discussion. $\omega_-(q)$ represents the frequency of the acoustic phonon branch, which vanishes for $q = 0$ (blue curve in Fig.2.2). As $q \to 0$ in Fig.2.2, ω_- is linear with respect to q and describes the motion of the two atoms in a unit cell as oscillating in phase with one another. Note that the slope $\frac{\partial \omega_-}{\partial q}$, in the limit $q \to 0$, is the velocity of sound in the solid. ω_+ represents the frequency of the optical phonon branch (red curve in Fig.2.2), and its value at $q = 0$ does not vanish. The neighboring atoms in this case oscillate out of phase and hence can carry a dipole moment if they are charged. It is this property that enables infrared light to couple to certain phonon modes giving rise to phonon-polariton phenomena.

2. Kinematics of Light Scattering and Conservation Laws

Consider a monochromatic light beam of frequency ω_1 with a propagation wave vector inside the crystal $|\vec{k}_1| = \frac{\omega_1 \times n_R(\omega_1)}{c}$, where c is the speed of light and n_R is the material's refractive index. Let the inelastic scattered photons have frequency ω_2 and a propagation wave vector $|\overrightarrow{k_2}| = \frac{\omega_2 \times n_R(\omega_2)}{c}$. It follows that the frequency and momenta of the scattering waves satisfy [2]

$$\omega = \omega_1 - \omega_2 = \pm\omega_j \qquad (2.\ 13)$$

$$\vec{k} = \overrightarrow{k_1} - \overrightarrow{k_2} = \pm\vec{q}_j. \qquad (2.\ 14)$$

ω_j and $\vec{q}_j$ correspond to the frequency and crystal momentum of the first-order type j crystal excitation in a material with perfect translation symmetry. The plus and minus signs correspond to Stokes (creation of one excitation) and anti-Stokes (annihilation of one excitation) scattering, respectively. The magnitude of the scattering wave vector is

$$|\vec{k}| = |\overrightarrow{q_j}| = \sqrt{|\overrightarrow{k_1}|^2 + |\overrightarrow{k_2}|^2 + 2|\overrightarrow{k_1}||\overrightarrow{k_2}|cos(\theta)}, \qquad (2.\ 15)$$

where θ is the angle between $\overrightarrow{k_1}$ and $\overrightarrow{k_2}$ as shown in Fig.2.3. For forward scattering ($\theta = 0$), $|\overrightarrow{k}|$ takes its minimum value of

$$|\vec{k}|_{min} = |\vec{k}_1| - |\vec{k}_2| = \frac{n_R(\omega_1)\,\omega_1 - n_R(\omega_2)\,\omega_2}{c}. \qquad (2.\ 16)$$

The largest value for $|\overrightarrow{k}|$ occurs in the back scattering geometry, when $\theta = 180^{\circ}$, and is

$$|\vec{k}|_{max} = |\vec{k}_1| + |\vec{k}_2| = \frac{n_R(\omega_1)\,\omega_1 + n_R(\omega_2)\,\omega_2}{c}. \qquad (2.\ 17)$$

It follows from Eq.2. 16 and Eq.2. 17 that in typical experiments performed in the visible and infrared spectral range, the scattering wave vector falls in the range $0 \leq |\vec{k}| \leq 10^6$ cm^{-1} [6]. This is very small relative to typical reciprocal lattice vectors at the edge of the Brillouin zone ($\sim 10^8$ cm^{-1}). Therefore, for first-order Raman processes, only elementary excitations at or near the center of the Brillouin zone Γ are accessible.

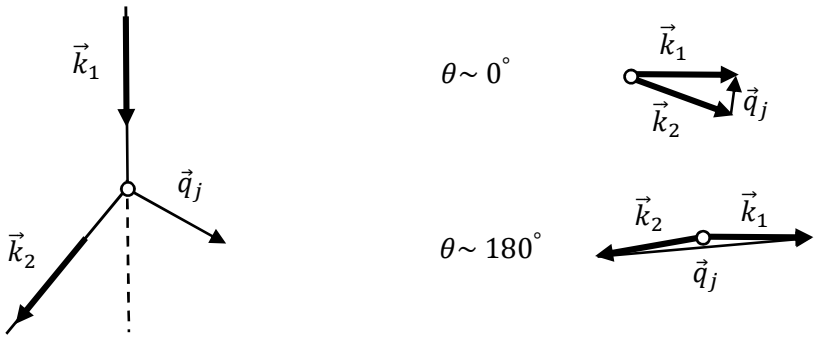

Figure 2.3: Wave vector diagrams for different scattering angles (Stokes scattering).

Eq.2. 14 breaks down, however, when 1) translational symmetry is lost, 2) the scattering volume is small or 3) the scattering medium is strongly absorbing. In the case that translational symmetry is lost, which occurs in mildly defected materials, solid solutions, alloys, and amorphous materials, crystal momentum is no longer conserved. This allows for light to access excitation states across the Brillouin zone resulting in the appearance of features that reflect the excitations' density of states in the Raman spectra. This property of inelastic scattering provides a powerful and non-destructive way to characterize the crystalline quality in materials [7]. Secondly, light scattering in materials that are small enough that the long-periodicity of the crystal is lost also relaxes the condition in Eq.2. 14 allowing for a range of excitations $\Delta \boldsymbol{q} \approx 2\pi/d$, where d is the crystal size [8]. Lastly, in strongly absorbing materials, the incident and scattered wave vectors, $\vec{k}_1$ and $\vec{k}_2$,

become complex and a range of elementary excitations ($\Delta q \sim Im(\vec{k}_1) + Im(\vec{k}_2)$) centered at $\vec{q} = Re(\vec{k}_1 - \vec{k}_2)$ are accessible [9,10].

3. Inelastic Scattering Cross Section

a) Macroscopic Theory

In this section we show a simple derivation of the classical cross section for inelastic light scattering. As in the previous section, consider incident and scattered light of frequencies, wave vectors, and electric fields $(\omega_1, \vec{k}_1, \vec{E}_1)$ and $(\omega_2, \vec{k}_2, \vec{E}_2)$, respectively. For an incident beam interacting with a volume V of a crystal, the cross section of the scattered light into a solid angle $d\Omega$ (as shown in Fig.2.4) is defined as

$$\frac{d\sigma}{d\Omega} = \frac{1}{I_1} * \frac{dI_2}{d\Omega}, \qquad (2.\ 18)$$

where I_2 and I_1 are the power of the collected and incident light, respectively. The incident electric field $\vec{E}_1 = \vec{E}_1^0 \cdot e^{i(\vec{k}_1 \cdot \vec{r} - \omega_1 t)}$ induces dipole moments, and the total dipole moment of the volume V is

$$\vec{P} = V\hat{\chi}\vec{E}_1 = V\hat{\chi}\vec{E}_1^0 \ e^{i(\vec{k}_1 \cdot \vec{r} - \omega_1 t)} \qquad (2.\ 19)$$

where $\hat{\chi}$ is the second-rank tensor electric susceptibility. In the case of Rayleigh scattering, $\hat{\chi}$ is constant and $\vec{P}$ oscillates at the frequency of the incident field; hence the scattered radiation has the same frequency ω_1. In addition, the radiation from the many dipoles in the volume V will interfere, and for flat samples this results in emission in only two directions, namely the reflected and the transmitted beams. In real materials, however, Rayleigh scattering is not the only scattering

process occurring. Inelastic scattering, although weak, also takes place and is emitted in all directions. The inelastic scattering, which is typically 10^{-7} less likely to occur compared to Rayleigh scattering [11], also contributes to the total electric susceptibility. Therefore, it can be treated as a perturbation in $\hat{\chi}$ due to the dipoles possessing their own resonant frequency ω_j. Hence, the electric susceptibility to first order in the atomic displacements can be written as

$$\hat{\chi} \approx \hat{\chi}_0 + \sum_i \frac{\partial \hat{\chi}(u_i)}{\partial u_i} u_i(\omega_1)\ e^{i(\vec{q}_j \cdot \vec{r} - \omega_j t)} \qquad (2.\ 20)$$

where $\hat{\chi}_0$ is the constant susceptibility responsible for Rayleigh scattering. The sum in the second term is taken over all cartesian coordinates *i*, with $\vec{q}_j$ representing the momentum of the excitation, as discussed in section 2.2. Here u_i are the cartesian components of the oscillation relative displacement ($\sum_i u_i^2$ is the square of the oscillation amplitude). The second term in Eq.2. 20 represents the first-order modulation-induced susceptibility, which when substituted into Eq.2. 19 gives

$$\vec{P}_2 = V \sum_i \frac{\partial \hat{\chi}(\omega_1, \omega_2)}{\partial u_i} \cdot \vec{E}_I^0\ u_i(\omega_I)\ e^{i\left((\vec{k}_1 \pm \vec{q}_j) \cdot \vec{r} - (\omega_1 \pm \omega_j)t\right)}, \qquad (2.\ 21)$$

Where the $\hat{\chi}$'s dependence on u_j is replaced with ω_1 and ω_2. ω_j can be determined from the frequency of the scattered light (Eq.2. 13). Note that the dipole oscillates at two frequencies, which results in emission at $\omega_2 = \omega_1 - \omega_j$ (Stokes) and at $\omega_2 = \omega_1 + \omega_j$ (anti-Stokes). However, Stokes scattering dominates, at room and low temperatures, due to low phonon populations [12]. This is the reason why experiments are usually carried out in the Stokes range.

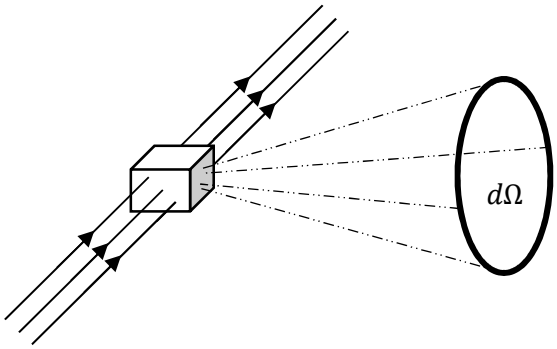

Figure 2.4: Diagram of a beam incident on a sample of volume V. $d\Omega$ is the solid angle in which the scattered light is collected.

In this work we only use light in the visible and infrared range, with wavelengths (> 400 nm) that are much larger than the dimensions of the cell (< 1 nm). In that case, the power emitted in the solid angle $d\Omega$ can be approximated by [13]

$$\frac{dI_2}{d\Omega} = \frac{1}{4\pi c^3} < \frac{d^2\vec{P}_2}{dt^2} > sin^2(\phi), \qquad (2.\ 22)$$

Where <> denotes the time average. Now, by utilizing Eq.2. 21, Eq.2. 22, and Eq.2. 18, we obtain the following cross section expression of the inelasticity scattered light

$$\frac{d\sigma_2}{d\Omega} = \frac{\omega_2^4 V}{(4\pi)^2 c^4} \left| \boldsymbol{e}_2 \cdot \frac{\partial \hat{\chi}(\omega_1,\omega_2)}{\partial u} \cdot \boldsymbol{e}_1 \right|^2 \cdot < u(\omega_1)^2 > \qquad (2.\ 23)$$

where $\boldsymbol{e}_2$ and $\boldsymbol{e}_1$ are the polarization unit vectors of the scattered and incident light, respectively. $< u(\omega_1)^2 >$ is the average square amplitude of the oscillation and $\frac{\partial \hat{\chi}}{\partial u} = \sum_i \frac{\partial \hat{\chi}}{\partial u_i}$. The dependence

of the cross section on the polarization of $\boldsymbol{e}_2$ and $\boldsymbol{e}_1$ provides a way to distinguish vibrational modes that possess different symmetries and experimentally assign their frequencies, as will be shown in later chapters.

b) Microscopic Theory

The microscopic method of deriving the cross section for inelastic scattering treats classical harmonic oscillations as states with discrete energy levels and the interaction of atoms with light are described in a matrix form of the interaction Hamiltonian. The microscopic theory provides a deeper understanding of the scattering mechanism which, for resonant scattering phenomena, for example, is the correct way to describe the process. The Raman cross-section relation for the microscopic theory is related to the quantum-mechanical transition rate $1/\tau$ through [12]

$$\frac{d^2\sigma}{d\omega_2 d\Omega} = \frac{n_R V}{nc} * \frac{d^2}{d\omega_2 d\Omega}\left(\frac{1}{\tau}\right), \qquad (2.\ 24)$$

where n is the number of incident photons and n_R is the refractive index of the medium for the incident light. $1/\tau$ is generally computed through time-dependent perturbation theory, as will be shown in the following section.

4. Raman Scattering in Crystals

As discussed earlier, the effects of light interactions with elementary excitations in a solid can be understood in the form of an induced polarization that oscillates at the frequency of the scattered photon. Therefore, the electric susceptibility can be expanded in powers of the elementary excitation coordinates. These excitation coordinates represent the relative atomic displacement of the atoms for optical phonons, stress resulting from acoustic phonons,

macroscopic electric fields due to infrared LO-phonons, etc. In non-polar materials and for optical phonons, the excitation coordinates are the normal mode coordinates ξ_i, where *i* notes the phonon type (we use notation of normal coordinates for consistency with the following section). Hence, the modulated electric susceptibility due to all phonon excitations with frequency and wave vector $(\omega_i, \boldsymbol{q})$ can be expressed as

$$\delta\hat{\chi} \approx \sum_i \frac{\partial \hat{\chi}}{\partial \xi_i}\xi_i + \sum_{ij} \frac{\partial^2 \hat{\chi}}{\partial \xi_i \partial \xi_j}\xi_i\,\xi_j + \cdots$$

$$\delta\hat{\chi} \approx \sum_i \hat{R}^i\,\xi_i(\boldsymbol{q}=0) + \sum_{ij,q_1q_2} \hat{R}^{ij}\xi_i(\boldsymbol{q_1})\xi_j(\boldsymbol{q_2}) + \cdots. \qquad (2.\ 25)$$

The first and second terms are the so called Raman tensor of first- and second-order, respectively. Since the scattering wave vector is much smaller than a reciprocal lattice vector, as stated earlier, the first-order Raman tensor can be approximated at $\boldsymbol{q}\sim 0$ and assumed to be independent of the wave vector. Note that in polar materials, however, and under resonant conditions, the first-order Raman tensor of infrared LO-phonons does depend on the crystal momentum due to the presence of the long-ranged macroscopic forces in the direction of the LO-phonons' propagation (Fröhlich interaction) [6]. The second term involves the scattering of two phonons of equal but opposite momenta $\boldsymbol{q_1} \approx -\boldsymbol{q_2}$. This results in features that closely follow the one-phonon density of states at twice the phonon frequency 2ω in the Raman spectra. In the following section, we briefly describe the microscopic theory of light scattering by optical phonons. We present a derivation of the first-order Raman tensor of a 3-dimensional non-polar diatomic crystal. We then discuss the significance of the Raman tensor on the resonant scattering behavior.

a) First-order Raman Scattering by Optical Phonons

The most important interaction in Raman scattering takes place through intermediate electronic transitions [12]. First-order Raman scattering involves three quantum processes: 1) absorption of a photon, 2) creation or destruction of a phonon, and 3) emission of a photon (see Fig.2.5 for example). These processes can occur in any time order. To show this, we start with the description of the quantum-mechanical Hamiltonian of a scattering medium which couples to the radiation field. The total Hamiltonian of the crystal is

$$\hat{H} = \hat{H}_0 + \hat{H}_{EL} + \hat{H}_{ER}\,, \tag{2. 26}$$

where $\hat{H}_{ER}$ is the Hamiltonian describing the electron-radiation interaction, $\hat{H}_{EL}$ is electron-lattice contribution, and $\hat{H}_0$ is the Hamiltonian of the unperturbed medium.

Introducing the creation ($a_{\boldsymbol{k}}^{+}$) and annihilation ($a_{\boldsymbol{k}}^{-}$) operators of photons with wave vector $\boldsymbol{k}$

$$< n_{\boldsymbol{k}} - 1|a_{\boldsymbol{k}}^{-}|n_{\boldsymbol{k}} >=< n_{\boldsymbol{k}}|a_{\boldsymbol{k}}^{+}|n_{\boldsymbol{k}} - 1 >= n_{\boldsymbol{k}}^{\frac{1}{2}}, \tag{2. 27}$$

where $n_{\boldsymbol{k}}$ is the total number of photons with wavevector $\boldsymbol{k}$. The electron-radiation Hamiltonian of electrons, with charge $-e$ and mass m, interacting with a radiation field was shown by Heitler [14] to have the form

$$H_{ER} \approx \frac{e}{m}\sum_j \sum_{\boldsymbol{k}} \left(\frac{2\pi\hbar}{\epsilon V \omega_{\boldsymbol{k}}}\right)^{\frac{1}{2}} [a_{\boldsymbol{k}}^{-} e^{i\boldsymbol{k}\cdot\boldsymbol{r}_j} + a_{\boldsymbol{k}}^{+} e^{-i\boldsymbol{k}\cdot\boldsymbol{r}_j}]\boldsymbol{\epsilon}_{\boldsymbol{k}} \cdot \boldsymbol{p}_{\boldsymbol{j}}, \tag{2. 28}$$

where $\boldsymbol{r}_j$ and $\boldsymbol{p}_j$ are the position and momentum of the j^{th} electron, $\boldsymbol{\epsilon}_{\boldsymbol{k}}$ is the unit vector parallel to the radiation's electric field, and ϵ is the medium's dielectric permittivity. The matrix elements $< \alpha|\hat{H}_{ER}|\beta >$, where $|\alpha >$ and $|\beta >$ are a pair of electronic states, are non-zero only when $|\alpha >$

and $|\beta >$ differ by only one electron or hole. We note that Eq.2. 28 is also true for some, but not all, other collective excitations, such as phonon-polariton, electron spin-flip and magnon excitations [15].

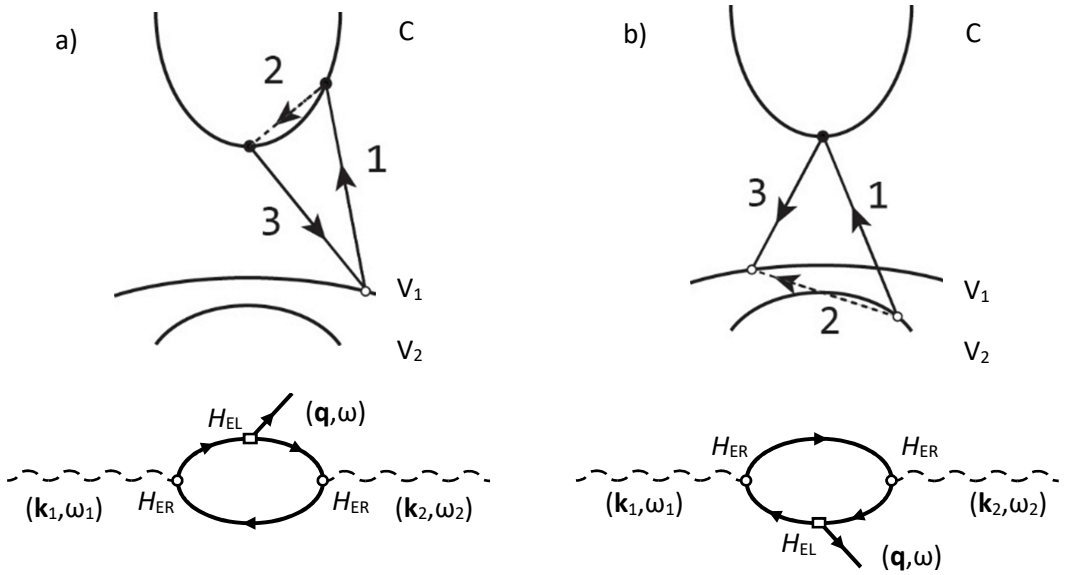

Figure 2.5: Energy band diagrams for light scattering processes from a filled valence band to an empty conduction band [7]. Below are their associated Feynman diagrams, where H_A and H_{EL} indicate the electron-radiation and electron-lattice interactions, respectively. (a) is the electron and (b) is the hole contributions [6].

In treating the electron-lattice Hamiltonian, we consider the case of non-polar crystals with two atoms, of masses M_1 and M_2, per unit cell – this problem was treated by Loudon in [16]. Here, the source of electron-lattice interactions stems from short-ranged dynamical forces due to atomic displacements. This leads to perturbations in the periodic electronic potential. The relative displacement due to optical phonons at a given position $\boldsymbol{R}$ is expressed by

$$\boldsymbol{\xi}(\boldsymbol{R}) = \left(\frac{\hbar}{2MN\omega_{s\boldsymbol{q}}}\right)^{\frac{1}{2}} \hat{\varsigma}_{s\boldsymbol{q}} e^{i\boldsymbol{q}\cdot\boldsymbol{R}}\left(b^{+}_{s-\boldsymbol{q}} + b^{-}_{s\boldsymbol{q}}\right), \quad \frac{1}{M} = \frac{1}{M_1} + \frac{1}{M_2}, \tag{2. 29}$$

where $b^{+}_{s\boldsymbol{q}}$ and $b^{-}_{s\boldsymbol{q}}$ are the creation and annihilation of the phonon in branch s with wave vector $\boldsymbol{q}$. $\omega_{s\boldsymbol{q}}$ is the frequency of the phonon, N is the number of unit cells in the crystal, and $\hat{\varsigma}_{s\boldsymbol{q}}$ is the unit vector in the direction of $\boldsymbol{q}$. It has been shown that the matrix elements of H_{EL} due to the atomic displacements relate to $\boldsymbol{\xi}$ and the deformation potential matrix elements $\Xi_{\alpha\beta}$ as follows [17]

$$< \alpha|H_{EL}|\beta >= \frac{\Xi^{i}_{\alpha\beta}\bar{\xi}_i}{a} \tag{2. 30}$$

where $\bar{\xi}$ is the same as in Eq.2. 29 without the exponent and a is the lattice constant. The deformation potential is the derivative of the perturbed periodic potential with respect to the atomic displacement. For polar crystals, it is necessary to consider an additional term in H_{EL} due to the long range Coulomb forces (Fröhlich interaction). Such interaction is a result of long-range forces produced by the longitudinal optical phonons. These long-range Coulomb forces are responsible for lifting the degeneracy in the energy of the phonon branches present in the case of non-polar crystals.

Now, the probability that at time t a photon $(\omega_1, \boldsymbol{k}_1)$ will be destroyed, and a phonon $(\omega_0, \boldsymbol{q})$ and photon $(\omega_2, \boldsymbol{k}_2)$ is created can be computed utilizing time dependent perturbation theory (to third-order) and can be described by the following expression (calculations are carried out in Loudon 1963 [16])

$$W(t) = \frac{2\pi t}{\hbar^6}\sum_{\boldsymbol{q},k_2}\sum_{\alpha\beta}\left|\frac{<n_1-1,1;n_0+1;0|H_I|a><a|H_I|b><b|H_I|n_1,0;n_0;0>}{(\omega_\alpha-\omega_1)(\omega_\beta-\omega_1)}\right|^2 \delta(\omega_1 - \omega_0 - \omega_2),$$

where $|a>$ and $|b>$ run over the complete sets of intermediate electronic states and $H_I = H_{ER} + H_{EL}$. $n_1, n_2\ and\ n_0$ are number of the incident photon, scattered photon, and created phonon, respectively.

Using Eq.2.28 and 2.30, assuming that the initial and final electronic states is the ground state, and summing over all intermediate states in electron-radiation and electron-lattice interactions that conserve momentum in each step of the process, the probability W reduces to

$$W(t) = \frac{4\pi^3 te^4}{\hbar^3 m^4 \epsilon^2 a^2 MN} \sum_{\boldsymbol{q},\boldsymbol{k}_2} \frac{n_1(n_0+1)}{\omega_0\omega_1\omega_2} \left|\hat{\varsigma}^i_{0\boldsymbol{q}} R^i_{12}(-\omega_1, \omega_2, \omega)\right|^2 \times \frac{(2\pi)^3}{V} \delta(\boldsymbol{k}_1 - \boldsymbol{q} - \boldsymbol{k}_2)\delta(\omega_1 - \omega_0 - \omega_2) \quad (2.31)$$

R^i_{12} is the Raman tensor given by

$$R^i_{12}(-\omega_1, \omega_2, \omega_0) = \frac{1}{V}\sum_{\alpha,\beta}\{\frac{p^2_{0\beta}\Xi^i_{\beta\alpha}p^1_{\alpha 0}}{(\omega_\beta + \omega_0 - \omega_1)(\omega_\alpha - \omega_1)} + \frac{p^1_{0\beta}\Xi^i_{\beta\alpha}p^2_{\alpha 0}}{(\omega_\beta + \omega_0 + \omega_2)(\omega_\alpha + \omega_2)} + \frac{p^2_{0\beta}p^1_{\beta\alpha}\Xi^i_{\alpha 0}}{(\omega_\beta + \omega_0 - \omega_1)(\omega_\alpha + \omega_0)} + \frac{p^1_{0\beta}p^2_{\beta\alpha}\Xi^i_{\alpha 0}}{(\omega_\beta + \omega_0 + \omega_2)(\omega_\alpha + \omega_0)} + \frac{\Xi^i_{0\beta}p^2_{\beta\alpha}p^1_{\alpha 0}}{(\omega_\beta + \omega_2 - \omega_1)(\omega_\alpha - \omega_1)} + \frac{\Xi^i_{0\beta}p^1_{\beta\alpha}p^2_{\alpha 0}}{(\omega_\beta + \omega_2 - \omega_1)(\omega_\alpha + \omega_2)}\} \quad (2.32)$$

The superscripts 1 (2) in the momentum matrix element p indicate the component of p along the polarization of the incident (scattered) light. The subscripts in the first-order Raman tensor indicate the directions of the light polarization. The negative sign in the left hand side of Eq.2. 32 is chosen so that the negative and positive frequency correspond to creation and annihilation of the appropriate photon and phonon. The structure of the Raman tensor is subject to the crystal symmetry transformations. Through group theory analysis, one can determine the non-zero tensor components. Rousseau *et al*. show a detailed step by step method of determining the normal modes' symmetries and their corresponding Raman tensors for arbitrary solids [18].

The delta function in Eq.2. 31, pertaining to the conservation of energy, is relaxed when the finite lifetime of the electrons and phonons are taken into account. It has been shown that the most important source of damping is due to the three-phonon anharmonic interaction [16], and hence the delta function is replaced with the Lorentzian

$$\frac{\Gamma}{(\omega_I-\omega_0-\omega_2-\Delta)^2+\Gamma^2}, \qquad (2.\ 33)$$

where Γ and Δ are constants that depend on the damping source. The probability, and hence the spectral line shape, has a Lorentzian shape centered at $\omega = \omega_I - \omega_0 - \Delta$ with a half width of Γ. In chapter IV, we will discuss the dependence of Δ and Γ on temperature. The corresponding increase in the phonon population leads to an increase of anharmonicity effects, which usually manifest themselves in the increase of Γ and |Δ| with increasing temperature. This increased anharmonicity introduces a shift in the frequency and a lifetime ($\tau \propto 1/\Gamma$) to the phonon.

The general form of the Raman tensor is very similar to Eq.2. 32, except that the deformation potential Ξ is replaced with the general electron-lattice Hamiltonian matrix element, which can include the Fröhlich interaction. In the case of uncorrelated electron-hole pairs, α and β denote

one-electron or hole intermediate states. And in the case of excitons, particularly Wannier excitons, it was shown that the results for the Raman tensor are essentially the same except that α and β are exciton states [19].

b) Resonant Raman Scattering

The correct way to describe resonant Raman scattering is by quantum mechanics due to the importance of the intermediate transitions' effects. Calculating cross sections for such scattering phenomena can be achieved by means of time-dependent perturbation theory as shown earlier in this section. Resonant Raman scattering occurs when the energy of the incident and/or scattered light is in the vicinity of an electronic transitions ($\omega_\alpha \approx \omega_1$ and/or $\omega_\beta \approx \omega_2$). In these conditions, the first term in Eq.2. 32 is the main contributor to the first-order Raman tensor as the denominator approaches zero. The order of the scattering process of the first term in Eq.2. 32 is, as shown in the diagram of Fig.2.5, as follows: (1) an incident photon is annihilated and an interband electron-hole pair is created through the electron-radiation interaction, (2) the pair excitation is then scattered by an optical phonon through the electron-lattice interaction and finally (3) the interband electron-hole pair is annihilated through the electron-radiation interaction creating the scattered photon.

In resonant inelastic scattering, it is convenient to separate the scattering processes in the summation of the first term on the right side of Eq.2. 32 into *two-* and *three-band* processes. The *two-band* and *three-band* terms involve intraband and interband matrix elements of the electron-lattice interaction, respectively. When the electron-hole pairs involve only two bands, $\omega_\alpha \approx \omega_\beta$, and in resonant conditions, both factors in the denominators approximately vanish. In electron-hole pair transitions involving three bands, however, ω_α and ω_β might differ greatly leading to

only one factor in the denominator of the resonant term vanishing while the contribution of the third and fifth terms in Eq.2. 32 become relevant. Therefore, *two-band* processes lead to stronger resonant behavior. However, if the two valence bands in the *three-band* scattering process are close ($\omega_\alpha \approx \omega_\beta$), the cross section due to the *two-* and *three-band* transitions have a similar resonant behavior [6].

In the case of uncorrelated electron-hole excitations in the intermediate states, the electron-radiation and electron-phonon interactions can be assumed to be nearly constant for the electronic bands considered. For fully symmetric phonon modes, modes which carry diagonal Raman tensors, and phonons in cubic materials, the *two-* and *three- band* contributions to the first-order transition susceptibility can be approximated as [6]

$$\delta\chi'_{\mu\nu}(\omega) = < C, V_{1,2}|H_{EL}|C, V_{1,2} > \frac{(\chi(\omega_1)-\chi(\omega_1-\omega))}{\hbar\omega} \qquad (2.\ 34.a)$$

$$\delta\chi''_{\mu\nu}(\omega) = < V_1|H_{EL}|V_2 > \frac{\chi^+(\omega_1)+\chi^+(\omega_1-\omega)-\chi^-(\omega_1)-\chi^-(\omega_1-\omega)}{2\Delta}, \qquad (2.\ 34.b)$$

where χ is the electric susceptibility, and for the second equation $\chi = \chi^+ + \chi^-$, $\chi^\pm$ are the contributions of the $V_{1,2}$ <-> C interband transitions. Δ is the energy difference between the two valence bands (V_1 and V_2). The electron-phonon matrix elements in Eq.2. 34 are due to the *two-* and *three-band* processes.

Evoking the quasi-static (or adiabatic) approximation ($\left|E_{\alpha,\beta} - \hbar\omega_1\right| \gg \hbar\omega$), which is valid for typical resonant scattering experiments where the electronic transitions and incident light have energies in the order of few eV, Eq.2. 34 reduce to

$$\delta\chi_{\mu\nu} =< C, V_{1,2}|H_{EL}|C, V_{1,2} > \frac{d\chi}{d(\hbar\omega_1)} \qquad (2.\ 35.a)$$

$$\delta\chi_{\mu\nu} =< V_1|H_{EL}|V_2 > \frac{\chi^+ + \chi^-}{\Delta}. \qquad (2.\ 35.b)$$

Eqs.2. 35 an approximate expression to calculate the resonant first-order Raman scattering intensity of optical phonons at $\boldsymbol{q} \approx 0$ from the frequency dependent electric susceptibility. As a matter of fact, this method has been used to generate the resonant curves of F_{2g} phonons in II-IV semiconductors [20] and in selenium and tellurium [21]. Ignoring three-band terms and using Eq.2. 35.a and Eq.2. 23, we arrive to the following approximate expression for the Raman cross-section of fully-symmetric *A* phonons as a function of excitation energy;

$$\sigma \propto \Xi_p^2 \left|\frac{d\chi}{d(\hbar\omega_1)}\right|^2 \omega_L^4, \qquad (2.\ 36)$$

where $\Xi_p \propto< C, V_{1,2}|H_{EL}|C, V_{1,2} >$ is the deformation-potential.

5. Fano-Interference

Fano-resonance is the interference between scattering amplitudes of discrete states and continua of excitations into which the discrete states decay. This interference arises from the alternative paths connecting the initial and final states of the system as displayed in Fig.2.6. For such resonance to occur, the discrete states and continua must overlap in energy and have the same symmetry. These interaction phenomena, treated by Fano [22], manifest themselves in asymmetric spectral line shapes; the profile which describes the interaction between one discrete states ϕ and one continua ψ_E has the following simple expression,

$$\sigma = \frac{(\frac{q\Gamma}{2} + \omega - \bar{\Omega})^2}{(\frac{\Gamma}{2})^2 + (\omega - \bar{\Omega})^2}, \qquad (2.\ 37)$$

where,

$$< \phi|H|\phi >= \hbar\Omega$$

$$< \psi_E|H|\phi >= V_E = \sqrt{\frac{\hbar\Gamma}{\pi}}$$

$$< \psi_{E'}|H|\psi_E >= E\ \delta(E - E'),$$

with $E = \hbar\omega$ and H being the Hamiltonian of the system. The asymmetry parameter q is proportional to the ratio of the two transition matrix elements ($q \propto T_{ph}/T_e$), which in the case of a phonon interacting with a continuum is the ratio of the two Raman scattering probabilities ($q \propto R_p/R_e$). The sign of q determines the direction of the asymmetry, and Γ is the spectral width. Here, $\overline{\Omega} = \Omega + \Delta_F$ (with Ω and Δ_F are the frequency of the discrete state and the shift in its corresponding peak due to the interference), where $\Delta_F = \Gamma/q$. Note that, as $|q| \to \infty$, the Lorentzian line shape is recovered and is centered at $\overline{\Omega} = \Omega$. In Raman scattering, the scattering amplitudes R_p and R_e, and hence q and Δ_F, exhibit a dependence on the excitation frequency. On the other hand, Γ is a constant electron-phonon coupling.

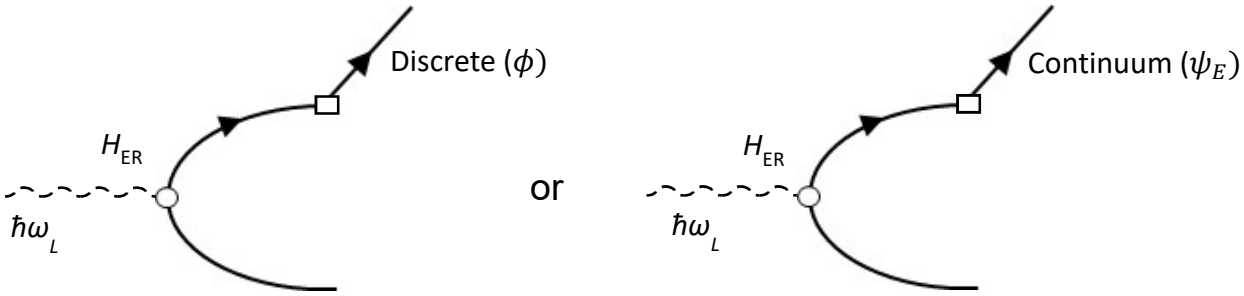

Figure 2.6: Diagrams showing two scattering processes of a coupled discrete state and continuum. The two states are interacting with the same radiation field.

6. Summary

In later chapters we will use the formalism that was presented here. Specifically, we utilize resonant Raman scattering to characterize the behavior of the cross-section of fully symmetric phonons as a function of the excitation frequency. We also characterize an asymmetric lineshape corresponding to a one-phonon mode as due to a Fano-resonance.

References

[1] P.M.A. Sherweed, Vibrational Spectroscopy of Solids, (Cambridge University Press 1972).

[2] J. M. Ziman, Principles of the Theory of Solids, 2nd ed. (Cambridge University Press 1972).

[3] H. Goldstein, C. Poole, J. Safko, Classical Mechanics, 3rd ed. (Addison-Wesley 2002).

[4] C. Kittel, Quantum Theory of Solids, (Wiley & Sons 1963).

[5] R. E. Peierls, Quantum Theory of Solids, (Oxford 1955).

[6] M. Cardona, Topics in Applied Physics: Light Scattering in Solids I (Springer-Verlag Berlin Heidelberg, 1983).

[7] W.H. Weber and R. Merlin (Eds), Material Science: Raman Scattering in Material Science (Springer-Verlag Berlin Heidelberg, 2000).

[8] F. H. Pollak, In Analytical Raman Spectroscopy, ed. By J. G. Grasselli and B. J. Bulkin (Wiley, New York 1991) Chap. 6, p. 137.

[9] D. L. Mills, A. A. Maradudin, E. Burstein, Ann Phys. (N.Y.) 56, 504 (1970).

[10] R. Zeyher, C. D. Ting, J. L. Birman, Phys. Rev. Letters 33, 908 (1974).

[11] D. C. Harris and M. D. Bertolucci, Symmetry and Spectroscopy (Dover Publications, 1989).

[12] W. Hayes and R. Loudon, Scattering of Light by Crystals (Dover Publications, 2012).

[13] J. D. Jackson, Classical Electrodynamics (Wiley, 2012) Chap. 9, p. 411.

[14] Heitler W. *The quantum theory of radiation*. Oxford, 1954.

[15] Loudon R. The Raman Effects in Crystals. *Adv. Phys.*, 50(7):813-864, 2001

[16] Loudon R. Theory of the first-order Raman effect in crystals. *Proc. R. Soc. Lond. A*, 275:218-232, 1963.

[17] Bir G. L. and Pikus G. E. Theory of the Deformation Potential for Semiconductors with Complex Band Structures. *Soviet. Phys. Solid State,* 2:2039, 1961.

[18] D. L. Rousseau, R. P. Bauman, and S. P. S. Porto, J. Raman Spectrosc. 10, 253 (1981).

[19] A. K. Ganguly, J. L. Birman, Phys. Rev. 162, 806, (1967)

[20] E. Anastassakis, C. H. Perry, Light Scattering in Solids, ed. By M. Balkanski (Flammarion Sciences Paris, 1971), p.70-71.

[21] W. Richter, J. Phys. Chem. Sol. 33, 2113 (1972).

[22] U. Fano, Phys. Rev. 124, 1866 (1961).

CHAPTER III

Experimental Procedures

This chapter describes the experimental equipment used in obtaining Raman scattering data as well as analysis methods which were used in resonant Raman scattering. We give a brief description on the excitation sources and measuring instruments utilized. Then we discuss methods employed to correct for apparatus parameters in our measurement of scattering cross-sections. Finally, fitting procedures are discussed.

1. Equipment:

a) Lasers

Access to lasers with various wavelengths is crucial in performing resonant Raman scattering. In this work, we use CW Argon, Ti:sapphire, and dye lasers. The Argon ion laser (Spectra Physics Beamlok 2060) was heavily used to either induce the Raman process or to pump another laser source (Ti:sapphire or dye laser). The CW Argon laser produces light in the green/blue region with narrow linewidths, down to 0.033 cm^{-1}. The wavelengths, from the Argon laser, which were most used are 514.5 nm, 496 nm, 488 nm, 476.5 nm, 457.9 nm and 453.5 nm. If used to pump another laser source, it is best to operate the Argon laser in the multiple-line configuration. In this configuration a broadband high reflector is used in order to achieve maximum total power. For wavelengths in the near-infrared region, we used a home built Ti:sapphire laser. It operates in the

range of 700 – 850 nm and its power peaks at ≈ 780 nm. A rhodamine dye laser was used to access wavelengths of 590 – 630 nm. The wavelength, from both Ti:sapphire and dye lasers, can be continuously tuned by a birefringent filter. Moreover, we used a monochromator to eliminate plasma lines in the case of the Argon laser, and narrow the linewidth of the beam produced by the dye and Ti:sapphire lasers.

b) Spectrometers

i. Single-Channel spectrometer (SPEX)

The SPEX (0.85m double SPEX 1404) is a double-grating spectrometer capable of achieving a fine resolution of 0.005 nm with a spectral coverage of 175 – 1040 nm. Unlike the Dilor XY multichannel spectrometer, described below, it is able to scan for large spectral regions continuously. It consist of two mechanically coupled holographic gratings (1800 grooves/mm), mirrors, four slits, as well as a water cooled photomultiplier tube (PMT) for signal collection. Fig.3.1 shows a schematic of the optical components of the instrument.

Light scattered from samples are collected and focused onto the entrance slit S1. Once in the spectrometer, the scattered light is diffracted by grating G1 and then directed towards the middle slits S2 and S3 to eliminate light from the laser beam. The light is sent to the second grating G2 for diffraction again, and the exit slit S4 selects the wavelength of the exiting photons, which are sent into the PMT. For each incident photon, the PMT generates a current pulse, which then is converted to a voltage and amplified with a high-gain video amplifier. This voltage is compared to a reference and, if above the PMT's background level, converted to a transistor-transistor logic pulse and sent to the counting electronics. The resolution is determined by the sizes of slit S1 and S4, which are set to be equal. A swingaway mirror M5 is used to switch between the two entrances.

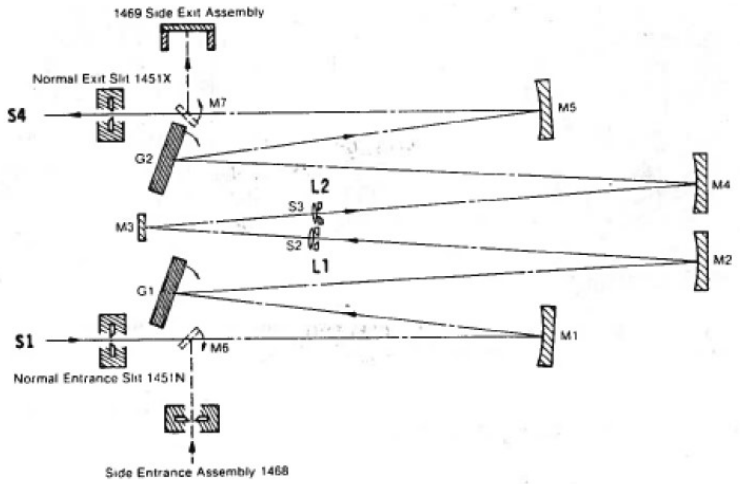

Figure 3.1: Schematic of optical components of the SPEX. M stands for Mirror, S for slit, and G for grating [1].

ii. Multi-Channel spectrometer (Dilor XY)

Most of the data presented in this thesis was obtained with a multi-channel Dilor XY spectrometer. A multichannel spectrometer consist of multiple detectors which enable one to measure a broad spectral range at once. The Dilor XY uses a charge-coupled device (CCD) camera, namely Synapse Horiba, which contains a 1024×256 pixel array and averages signal from pixels on the same column at each frequency. The CCD operates at liquid nitrogen temperatures to reduce background noise. The drawbacks to this type of light detection lie in the resolution limit imposed by the finite detector size and in the difficulty in scanning spectral regions larger than the detection array.

The Dilor is a triple-grating spectrometer, which can be used in several configurations. In the double-subtractive configuration, the first two gratings (G1 and G2 from Fig.3.2), which are coupled, along with the middle slit (S2) determine the spectral window which is then passed to the third grating (G3). Afterwards, the third grading disperses the light across the charge-coupled device (CCD) camera, which is attached at the end of the optical path after the exit slit (S3). This

configuration provides excellent Rayleigh light rejection. For our experiments, however, we only use the "normal" configuration in which the middle slit S2 is completely open. This was so because the spectral regions we measured were far enough from the Rayleigh light that the subtractive configuration was not needed. If one seeks higher resolution, the Dilor can be used in the high definition configuration. This configuration extends the optical path allowing light to disperse more after going through G3 and before reaching the CCD camera. The resolution of the instrument is determined by the entrance (S1) and exit (S3) slits. In our experiments, S1 and S3 were set to 200 nm. We used the spectrometer in the normal configuration. And if more resolution was needed, we used the high definition configuration.

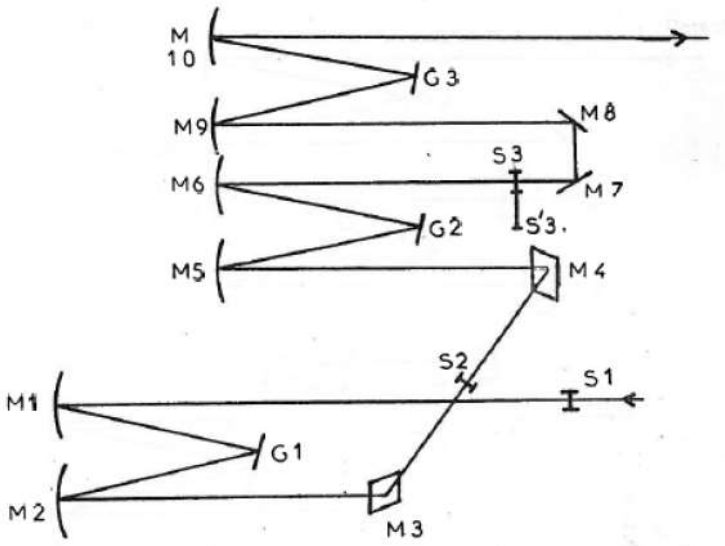

Figure 3.2: Schematic of optical components in the Dilor. M, refers to mirror, S to slit, and G to grating [2].

2. Data Analysis of Resonant Raman Scattering Experiments

In evaluating the scattering cross-section of phonons in our experiments (chapter V), we corrected for losses due to measuring apparatus and the sample's optical constants. Losses from the spectrometer are due to optical components within the instrument, gratings, mirrors, CCD camera, *etc.*, all of which have efficiencies that depend on the wavelength. Losses due to reflection and the scattering volume of the material must also be taken into account. This problem has been treated by Richter [3], who showed that for experiments performed on opaque bulk materials in the backscattering geometry, the corrected scattering cross-section is

$$d\sigma \propto S \frac{K}{(1-R)^2} * \frac{1}{f} * \frac{1}{I_L}$$

where R and K are the reflectivity and absorption constant of the material, f is the response function of the instrument, S is the cross-section before corrections, and I_L is the intensity of the incident beam – this is necessary if I_L is different for different measurements.

a) Instrument's Response

To obtain the response function of the instrument, we utilized a black body light source with a known emission spectrum. The black body light source used was a commercial halogen lamp (Ocean optics HL-2000-CAL), whose spectral output was provided by the factory. We illuminated the lamp into the spectrometer (Dilor XY) with a polarizer placed in between such that the polarization of light entering the spectrometer is vertical (perpendicular to the entrance slit). The spectrum over the range in which Raman scattering experiments were carried out (450 - 850 nm) was recorded (see Fig.3.3). We fitted the spectrum to a polynomial function then divided by the known (real) spectrum of the lamp (also shown in Fig.3.3). The resulting response function of the instrument of light with vertical polarization is shown in Fig.3.4.

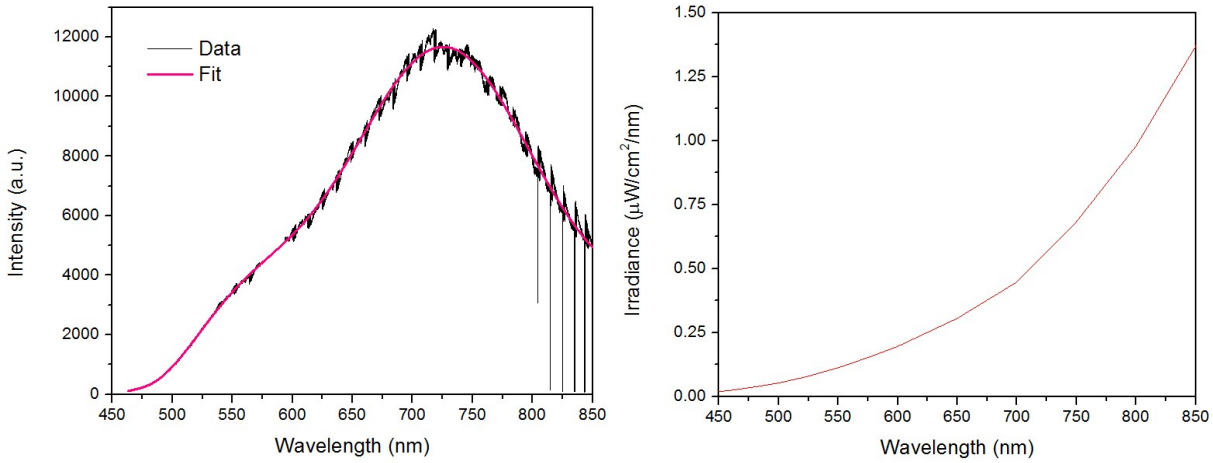

Figure 3.3: Spectrum of white lamp (black body) obtained by Dilor with the light polarization being perpendicular to the entrance slit (on the left) and the known spectrum of the lamp provided by the factory (on the right).

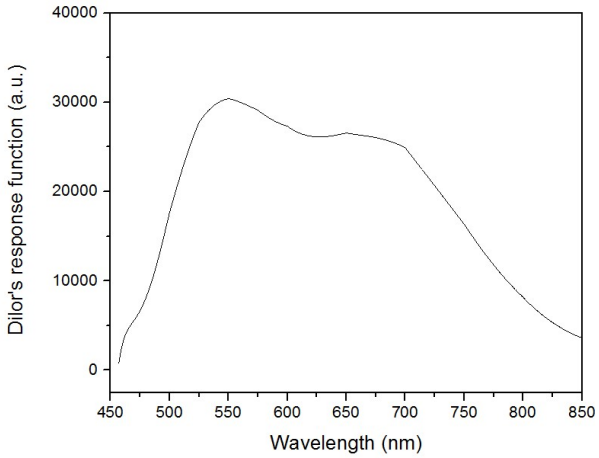

Figure 3.4: Response of spectrometer (Dilor XY), which was used in resonant Raman scattering experiments (chapter V) to correct for spectrometer losses in the cross-section of phonons. The polarization of the incident light is perpendicular to the entrance slit S1.

b) Correcting for Reflection and Absorption losses

As stated in chapter V, we show data of cross-sections of phonons in Bi_2Se_3 at 10 K. In correcting for losses due to reflection and absorption, we utilized room temperature optical constants because low temperature capabilities were not available. Here we argue that these corrections do not change significantly with respect to temperature.

Room temperature optical constant were measured through ellipsometry. To compare these results with values at 10K, we performed reflection measurements with respect to the angle of the incident light at selected wavelengths. We then fitted the results to Fresnel's equations. Fig.3.5 shows reflection measurements at 10 K performed with wavelengths 488 and 647 nm of the S- and P-polarized light - note the good quality of the fits. Now, the results of penetration depth ($1/K$) measured through reflection at 10 K and through ellipsometry at room temperature is presented in Fig.3.6. It is clear that the change in penetration depth with respect to temperature (in the range of 10 to 300 K) is insignificant, hence the scattering volume in approximately the same.

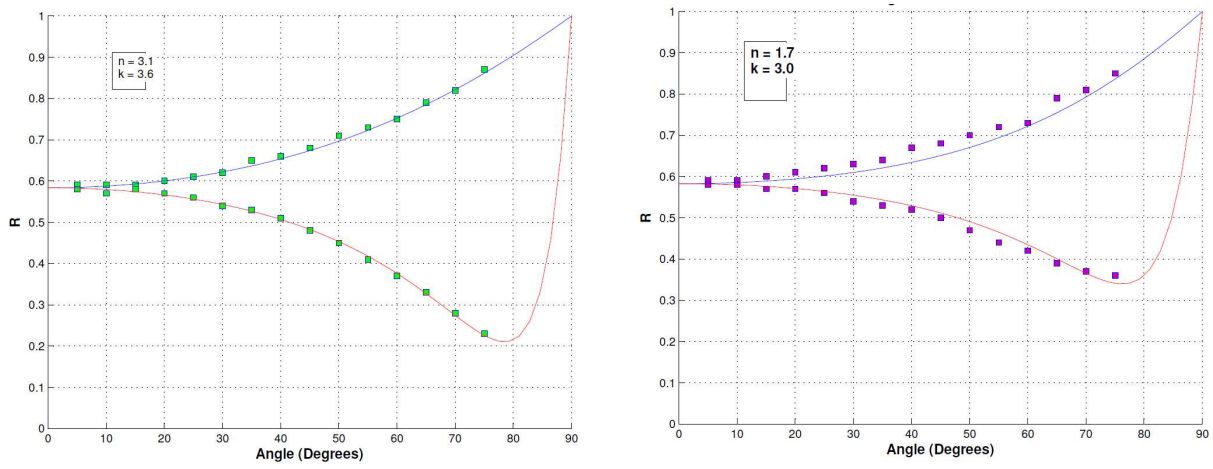

Figure 3.5: Reflection measurements with respect to the angle of the incident beam in Bi_2Se_3 at 10K. On the left is the reflectivity at 488 nm and on the right at 647 nm

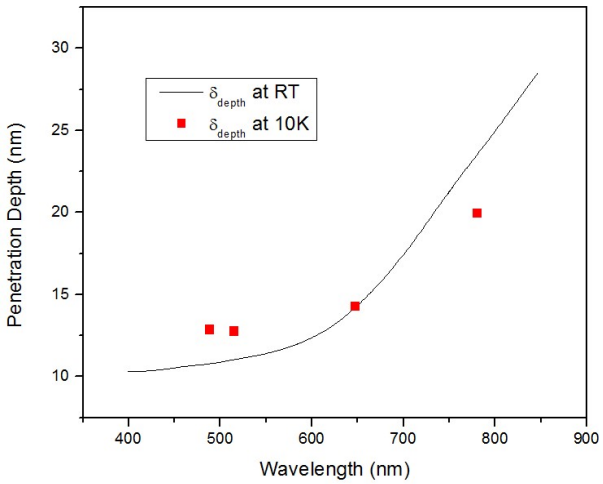

Figure 3.6: Penetration depth obtained by Fresnel's equations at 10 K (red dots) and by ellipsometry (solid curve).

We also used the ellipsometry data to obtain the theoretical curve of the cross-section of the A-symmetry phonons as a function of the excitation energy ω_L (σ vs ω_L). Since the theoretical expression involves the derivative of the dielectric constant ε ($\sigma \propto \left\|\frac{\partial \varepsilon}{\partial \omega_L}\right\|^2$, see Eq.2.35.a), we are more concerned with the trend of ε as the temperature changes. Fig.3.7 shows the squared of the amplitude of the dielectric constant with respect to wavelength at room temperature and 10 K – the data at 10 K is multiplied by a constant. The data at both temperatures exhibit the same trend and hence justifies using room temperature data to predict cross-sections of A-like phonons at 10K.

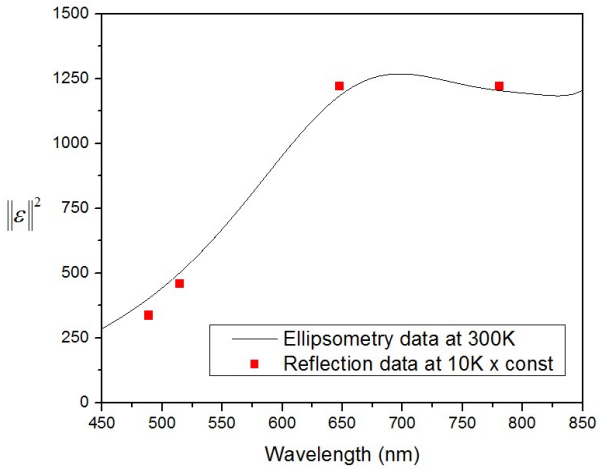

Figure 3.7: The squared amplitude of the dielectric constant acquired through ellipsometry at 300 K (solid line) and reflection measurements at 10 K (red dots) – low temperature data is multiplied by a constant.

3. Fitting Procedures

As will be mentioned in chapter V, we fitted an asymmetric peak in the Raman spectra of Bi_2Se_3 to a Fano-expression (Eq.2.44). The fitting procedure involved fitting other peaks as well as convoluting Eq.2.44 with the spectrometer's response to account for the instrument's resolution. Fig.3.8 shows a Raman spectrum of Bi_2Se_3 at 10 K obtained in the backscattering geometry with excitation wavelengths 808 and 764 nm. Fig.3.8 shows two large peaks corresponding to bulk E_g^2 and A_{1g}^2 (see chapter IV for details). The additional peak called β, studied elsewhere by Kung *el al*., corresponds to a surface resonance (see [4]). The peak showing an asymmetric profile and labeled as surface phonon is the peak we sought to fit. We do this for spectra at various excitation energies.

The shoulder of the peaks β and A_{1g}^2 contribute to the cross-section of the right side of the profile of the surface phonon. Therefore, for more accurate fits of the asymmetric profile, we took into

account the β and A_{1g}^2 modes. We performed a piece by piece fit. First, we fitted the A_{1g}^2 mode to a Lorentzian function in the range 175 - 185 cm^{-1}, then the β peak in the range 165 to 175 cm^{-1}. We found that spectral width of the A_{1g}^2 and β peaks are constants in all spectra regardless of the excitation line. Finally, we added the Fano-expression to the two obtained Lorentzian functions to fit the asymmetric peak. Initial fits to the symmetric profile in spectra obtained with all excitation energies were performed to obtain an average value of the spectral width. Then we performed the fit again with the spectral with being constant (4.1 cm^{-1}).

All expressions were convolved prior to fitting to consider for the spectrometer's resolution. The following expression was used

$$\sigma = A \int g(\omega - \omega') \cdot f(\omega') d\omega'$$

where g is the spectrometer's response to a delta function (resolution), f is the Lorentzian or Fano expression.

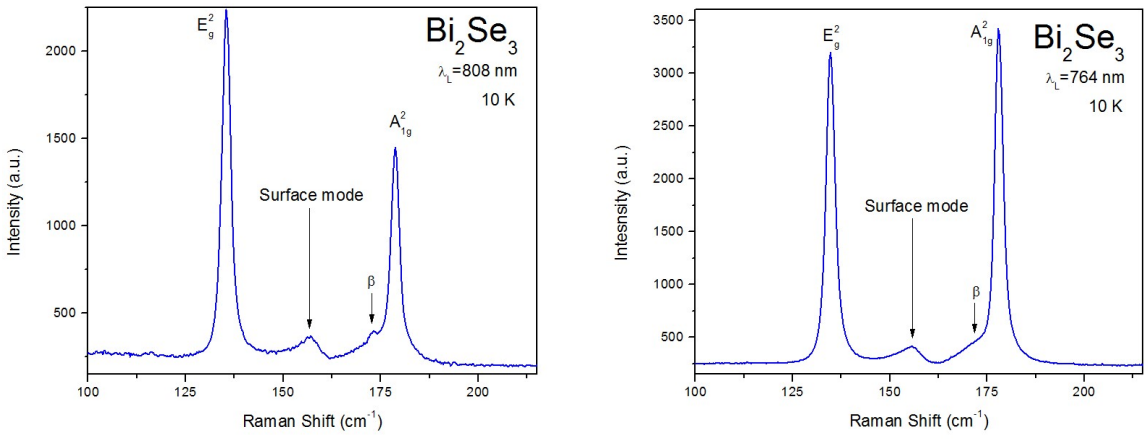

Figure 3.8: Raman spectra of Bi_2Se_3 at 10 K for excitation wavelengths 808 nm (left) and 764 nm (right).

References

[1] SPEX Operation & Maintenance Instructions (Industries, Inc., Metuchen, New Jersey, 1981).

[2] User Manual Dilor XY Modular Laser Raman Spectrometer (Instruments S. A. Jobin Yvon, Edison New Jersey).

[3] W. Richter, Springer Tracts mod. Phys. 78, 121 (1976)

[4] H. -H. Kung, M. Salehi, I. Boulares, A. F. Kemper, N. Koirala, M. Brahlek, P. Lošťák, C. Uher, R. Merlin, X. Wang, S.-W. Cheong, S. Oh, and G. Blumberg, Phys. Rev. B 95, 245406 (2017).

CHAPTER IV

Observation of Surface Phonons in the Topological Insulators Bi_2Se_3 and Bi_2Te_3

Bi_2Se_3 and Bi_2Te_3 are layered compounds, which have been extensively studied in the past due to their exceptional thermoelectric properties [1]. They were also among the first compounds identified as three-dimensional topological insulators [2,3,4,5]. Because of its crucial relevance to their surface conductivity properties, the study of electron-phonon coupling [6] and, moreover, the search for vibrations localized at the surface, have been the subject of many studies in recent years [7,8,9,10]. In particular, inelastic helium scattering [7,8], surface enhanced Raman scattering [9] and time-resolved photoemission measurements [10] in Bi_2Se_3 and Bi_2Te_3 show features that were attributed to surface modes as well as strong electron-phonon coupling at the surface. Also, weak features observed in Raman spectra were attributed to surface effects unrelated to the topological surface states [11].

In this chapter, we present experimental results on the temperature- and excitation-wavelength (λ_L–) dependence of Raman scattering, for bulk Bi_2Se_3 and Bi_2Te_3. Other than the expected, and previously reported Raman-active bulk modes [12,13], we find weak peaks at low temperatures in both compounds, which we ascribe to surface vibrational modes. These peaks were previously

observed in both compounds in thin-film [11,14,15,16,17,18,19,20,21,22] and bulk Bi_2Se_3 [22,23] and were assigned to infrared Raman forbidden bulk modes. We show such assignment to be incorrect and present experimental evidence of their surface nature. We will also present density functional theory calculations, which support our assignment. These calculations, which do not consider spin-orbit coupling, reveal a pair of surface-modes, the lower-frequency of which is very close in frequency to the peaks found in the Raman experiments. Arguments are also given suggesting that spin-orbit effects are not important in determining the structural properties and phonon dispersion in these materials.

Local density approximation calculations were performed by our collaborators Professor Emmanouil Kioupakis and Guangsha Shi, at the time a graduate student, from the Material Science Department at the University of Michigan. The work presented in this chapter is published in Solid State Communications [24].

1. Topological Insulators

Topological insulators (TIs) are a new class of materials that are insulating in the bulk but exhibit metallic surfaces, which arise from strong spin-orbit coupling and particular properties of their band structure. The electronic surface states of TIs consist of gapless bands characterized by a linear (Dirac) dispersion, which are protected against backscattering from time-reversal invariant defects and impurities [25,26]. Such properties were first predicted and experimentally verified in the alloy Bi_xSb_{1-x} in 2007 and 2008, respectively [2,3,4,5]. Soon after that, second-generation topological insulators, which included Bi_2Se_3 and Bi_2Te_3, were discovered experimentally through angle-resolved photoemission measurements (ARPES) [2]. Fig.4.1 shows ARPES data for Bi_2Se_3 and Bi_2Te_3 showing gapless Dirac surface states, a direct evidence of their topological properties.

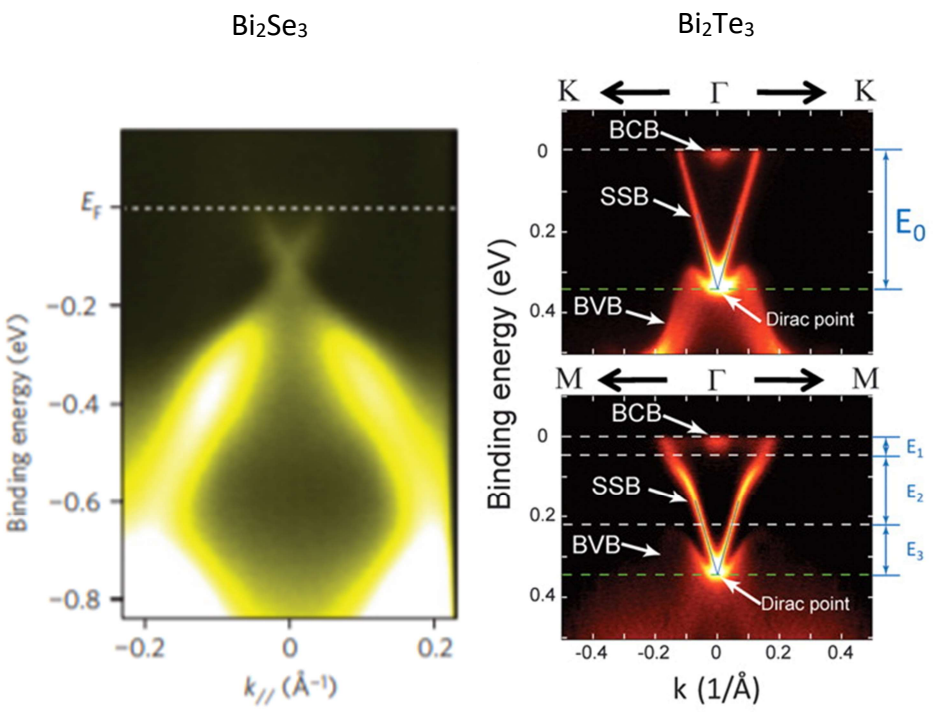

Figure 4.1: Energy dispersion bands along various high symmetry lines obtained from ARPES for Bi_2Se_3 (on the left, in yellow) [4] and Bi_2Te_3 (on the right, in red) [5]. On the right, BCB and BVB stand for bulk conduction and valence band, respectively, and SSB stands for surface state band. The top dotted horizontal line in all figures indicate the Fermi energy (E_F on the left and 0 on the right)

In recent years these novel materials have attracted significant interest, not only due to their unique electronic properties, but also because they hold promise for applications in quantum computing [26,27] and spintronic [28], as well as terahertz detection [29], thermoelectric [30] and tunable nonlinear optical devices [31].

2. Crystal Structure and Lattice Dynamics of Bi_2Se_3 and Bi_2Te_3

Both Bi_2Se_3 and Bi_2Te_3 crystalize in the space group $R\bar{3}m$, with point group D_{3d}. They both have the same rhombohedral structure and contain 5 atoms in a unit cell (see Fig.4.2.b). They are formed by the stacking of hexagonal monolayers of either Bi or Se/Te in a close-packed fcc fashion [32]. A quintuple layer is a sequence of five monolayer planes in the order X-Bi-X-Bi-X, where X = Se, Te (Fig.4.2). The bonding between the monolayers is covalent within a quintuple layer; however, the quintuple layers are held by weak van der Waal forces. The Brillouin zone is shown in Fig.4.2.c where the high symmetry points are highlighted.

With 5 atoms per unit cell, Bi_2Se_3 and Bi_2Te_3 have 15 vibrational phonon branches, 3 of which are acoustic. The irreducible representations of the 12 optical modes at the center of the Brillouin zone are:

$$\Gamma = 2E_g + 2A_{1g} + 2E_u + 2A_{1u},$$

where $2E_g + 2A_{1g}$ and $2E_u + 2A_{1u}$ are, respectively, Raman and infrared-active representations [12]. Note that due to the inversion symmetry in the crystal, Raman modes are infrared forbidden and vice versa. *E* modes are doubly degenerate and *A* modes are fully symmetric. *A* and *E* modes oscillate along and perpendicular to the $\hat{c}$ axis, respectively (Fig.4.3).

Below are the Raman tensors for the Raman modes:

$$R(A_{1g}) \equiv \begin{pmatrix} a & 0 & 0 \\ 0 & a & 0 \\ 0 & 0 & b \end{pmatrix},\ R(E_g^1) \equiv \begin{pmatrix} 0 & e & 0 \\ e & 0 & d \\ 0 & 0 & d \end{pmatrix},\ R(E_g^2) \equiv \begin{pmatrix} e & 0 & -d \\ 0 & -e & 0 \\ 0 & -d & 0 \end{pmatrix}.$$

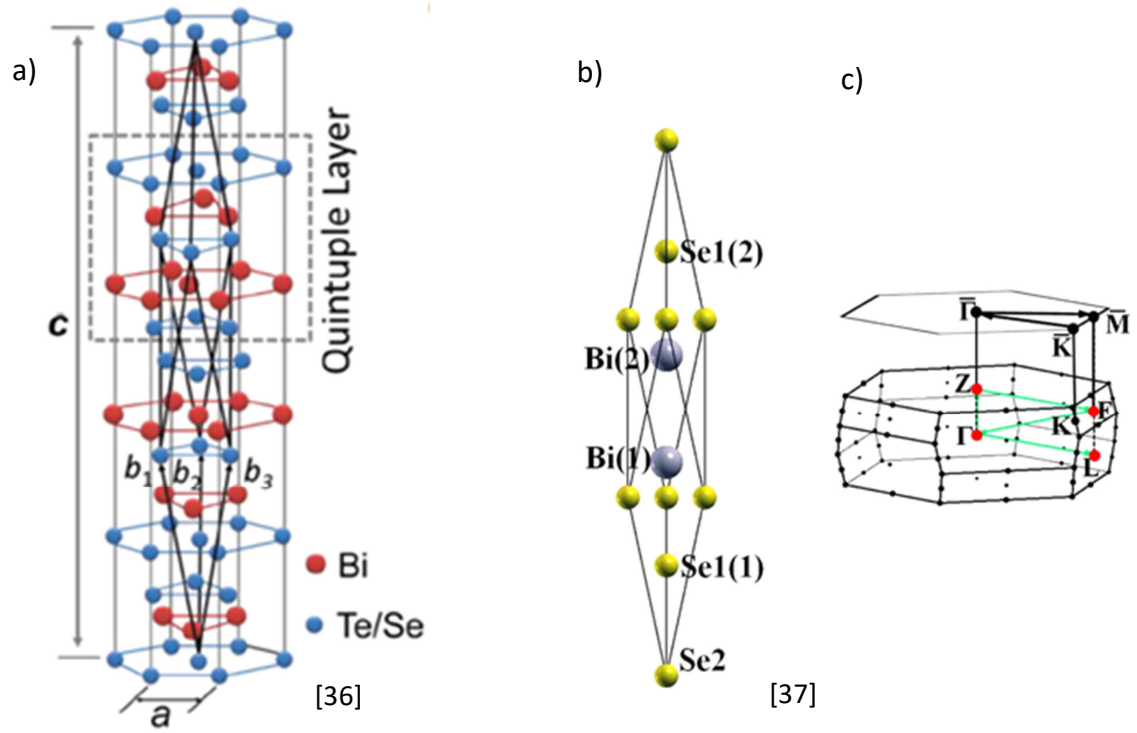

Figure 4.2: (a) Crystal structure of Bi_2Se_3 and Bi_2Te_3. A quintuple layer consist of five fundamental atomic planes [33]. (b) Rhombohedral unit cell of Bi_2Se_3, where Se1 and Se2 refer to two non-equivalent atomic positions [32]. (c) The first Brillouin zone with high symmetry points and lines [32].

Note that in the backscattering geometry, where the scattering wave vector is along the $\hat{c}$ axis, the intensity of the peak corresponding to A_{1g} modes is $\propto a^2\cos(\theta)$, where θ is the angle between the polarization of the incident and the scattered light. The peak corresponding to the E_g modes is always present and its intensity has no dependence on θ.

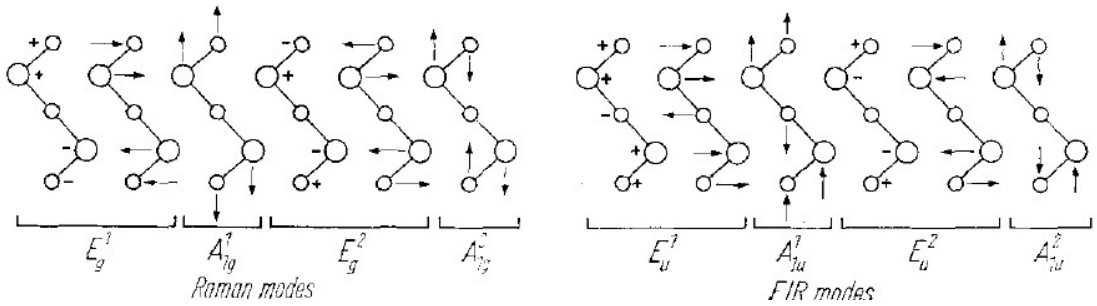

Figure 4.3: Atomic displacements of the zone center vibrational modes of Bi_2Se_3 and Bi_2Se_3 [13]

Bulk optical phonons of Bi_2Se_3 and Bi_2Te_3 have been previously measured using Raman [13, 34, 35, 36], neutron scattering [37], and infrared spectroscopy [13,38]. In Bi_2Te_3, however, we report here low-temperature Raman spectra for the first time.

3. Raman Scattering

a) Experimental Methods

Raman spectra were obtained in the backscattering geometry $z(x, x\ or\ y)\bar{z}$ with the scattering wavevector along the $\hat{c}$ axis. To select the polarization of the scattered light, a polarizer was placed before the triple grating spectrometer (Dilor XY) whose entrance and exit slits were set at 200 μm. The spectra were imaged on a CCD camera (Synapse Horiba). As sources, we employed an argon ion laser, a rhodamine and DCM dye laser and a Ti:sapphire cw laser. A prism-based monochromator was used to filter the Argon plasma lines and also narrow down the broad Ti:sapphire and dye spectrum. We performed the measurements at temperatures in the range 10 - 130 K. Prior to each measurement, the samples were cleaved in air and immediately placed under vacuum in a Janis ST-300 cryostat – this insures that defect-induced band bending near the surface due to air exposure is insignificant [39].

The crystals were grown by the Bridgman-Stockbarger technique, which produces n-type Bi_2Se_3 crystals due to the naturally formed Se vacancies [40] and p-type Bi_2Te_3 [41]. Samples were characterized by Trevor Bailey, in Professor Uher's laboratory, through Hall effect measurements to have carrier concentrations of $\approx 2.9 \times 10^{19}$ and 1.8×10^{19} cm^{-3} at 10 K for Bi_2Se_3 and Bi_2Te_3, respectively. At $n \approx 2.9 \times 10^{19}$ cm^{-1}, for Bi_2Se_3, the Fermi energy is $E_F \approx 250$ meV above the Dirac point [42].

b) Raman Data and Discussion

Fig.4.4 shows Raman spectra of Bi_2Se_3 and Bi_2Te_3 at various temperatures in the $z(yy)\bar{z}$ ($A_g + E_g$) scattering configuration; note the logarithmic scale. Consistent with previous reports [13,43], the bulk Raman-active modes at 10 K are at 38.5 cm^{-1} (E_g^1), 75.5 cm^{-1} (A_{1g}^1), 135.8 cm^{-1} (E_g^2) and 178.2 cm^{-1} (A_{1g}^2) for Bi_2Se_3 and 64.1 cm^{-1} (A_{1g}^1) 106.1 cm^{-1} (E_g^2) and 139.0 cm^{-1} (A_{1g}^2) for Bi_2Te_3; see Table I. The spectra in the insets were obtained in the E_g (red, top) and $E_g + A_g$ (blue, bottom) configurations. The peak we attribute to a surface phonon is the weak feature which appears between the E_g^2 and A_{1g}^2 modes at 159 cm^{-1} and 114 cm^{-1} for Bi_2Se_3 and Bi_2Te_3, respectively. This peak has been previously observed in thin films and few-monolayer samples of both compounds [11,14,15,16,17,18,19,20,21,22] and in single crystals of Bi_2Se_3 [22,23] but never before in bulk Bi_2Te_3. Note that these prior studies detected numerous other weak features in both compounds that were not observed in the present work.

Symmetry	Bi_2Se_3			Bi_2Te_3		
	Experiment	Theory		Experiment	Theory	
		This work	LDA+SOC [55]		This work	LDA+SOC [55]
E_g^1	39^+	45	43	--	43	42
A_{1g}^1	75^+	75	75	64^+	65	63
E_g^2	136^+	143	138	106^+	113	105
A_{1g}^2	178^+	183	175	139^+	142	132
E_u^1 (TO)	61*	90	82	48*	71	64
E_u^1 (LO)	117**	133	--	86**	99	--
A_{1u}^1 (TO)	--	145	137	88*	105	97
A_{1u}^1 (LO)	--	158	--	98**	114	--
E_u^2 (TO)	134*	136	131	98*	101	95
E_u^2 (LO)	138**	158	--	100**	116	--
A_{1u}^2 (TO)	--	166	163	114*	128	121
A_{1u}^2 (LO)	--	173	--	124**	134	--

Table 1: Experimental and theoretical values of Raman and infrared bulk phonon frequencies for Bi_2Se_3 and Bi_2Te_3 in units of cm^{-1}. Theoretical values including spin-orbit coupling (SOC) are from [44]. Experimental Raman ($^+$) and infrared (*) [13] values were measured at 10 K and 15 K, respectively. Frequencies of the LO components of infrared-active phonons (**) were extracted from infrared reflectivity data using a single-oscillator model. Values for Bi_2Te_3 are in excellent agreement with inelastic neutron scattering results [37]. Theoretical work was done by Guangsha Shi and professor Emmanouil Kioupakis from the Material Science Department at the University of Michigan. See section 4.

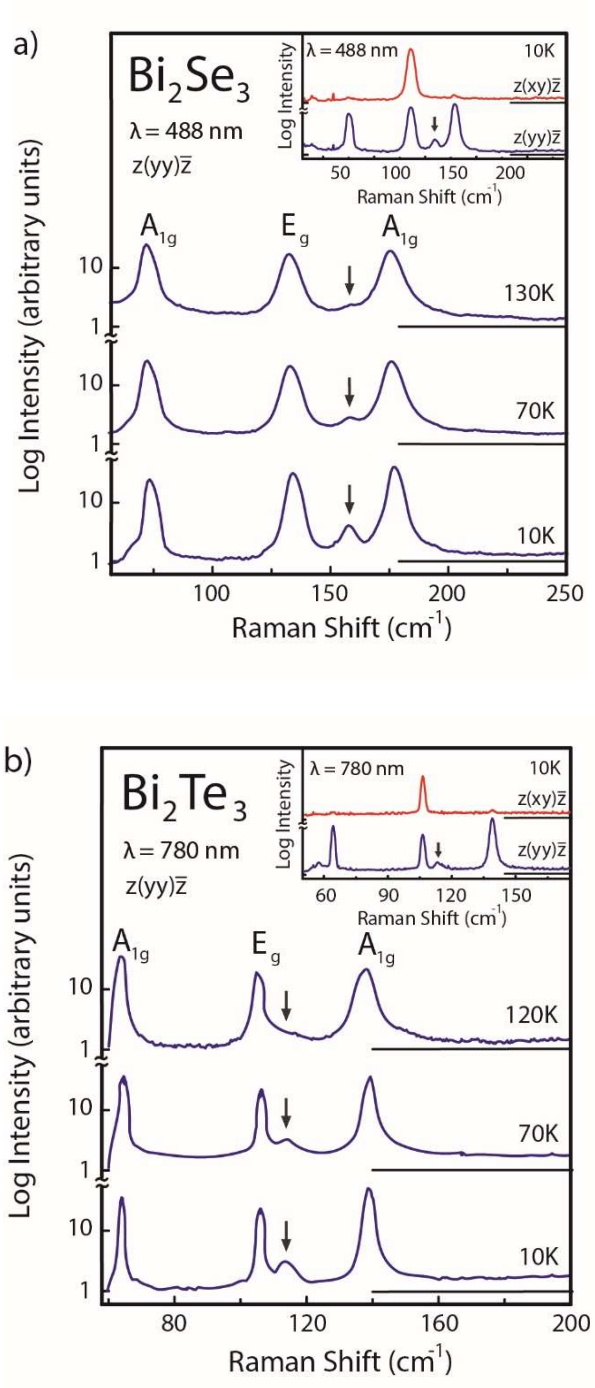

Figure 4.4: Raman spectra of (a) Bi_2Se_3, 488nm excitation, and (b) Bi_2Te_3, 780nm excitation, at various temperatures. Selection rules are shown in the insets. The intensity scale is logarithmic for all the traces. Arrows denote the surface mode.

The peak we assign to a surface phonon appears only in the *A* scattering representation, and is strongest at 10 K. In both compounds, the peak intensity decreases with increasing temperature and nearly vanishes above 130 K, whereas the behavior of the integrated intensity in Bi_2Te_3 follows closely that of bulk modes, see Fig.4.5. Fig.4.6 shows Raman spectra at 10 K at various excitation wavelengths; the intensity scale is linear. Note the surface mode in both compounds is present at all wavelengths. The Raman cross section for the extra peak depends weakly on λ_L in that it varies by less than one order of magnitude in the range 1.6 - 2.5 eV; see chapter V. Consistent with allowed Raman scattering [45], the cross section of the A_{1g} bulk modes varies as $\omega^4|d\varepsilon/d\omega|^2$, where ω is the laser frequency and $\varepsilon(\omega)$ is the permittivity (more on this in chapter V). The inset in Fig. 4.6 (a) shows an enlarged view of the λ_L = 780 nm spectrum. The surface phonon clearly shows an asymmetric lineshape, which we attribute to Fano-type interference due to coupling to an electronic continuum [46] – This will also be addressed in chapter V.

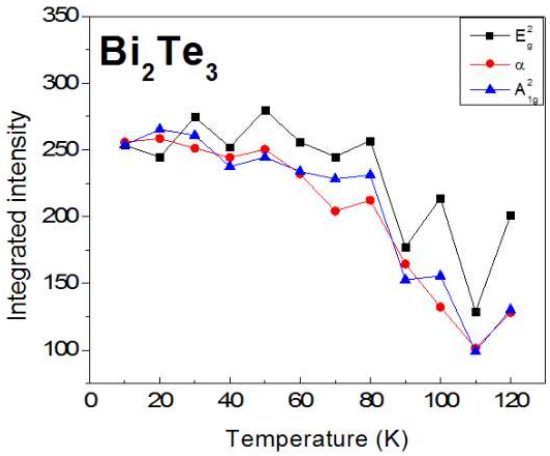

Figure 4.5: Normalized integrated intensity of the surface mode (α) and the Raman bulk modes E_g^2 and A_{1g}^2 in Bi_2Te_3.

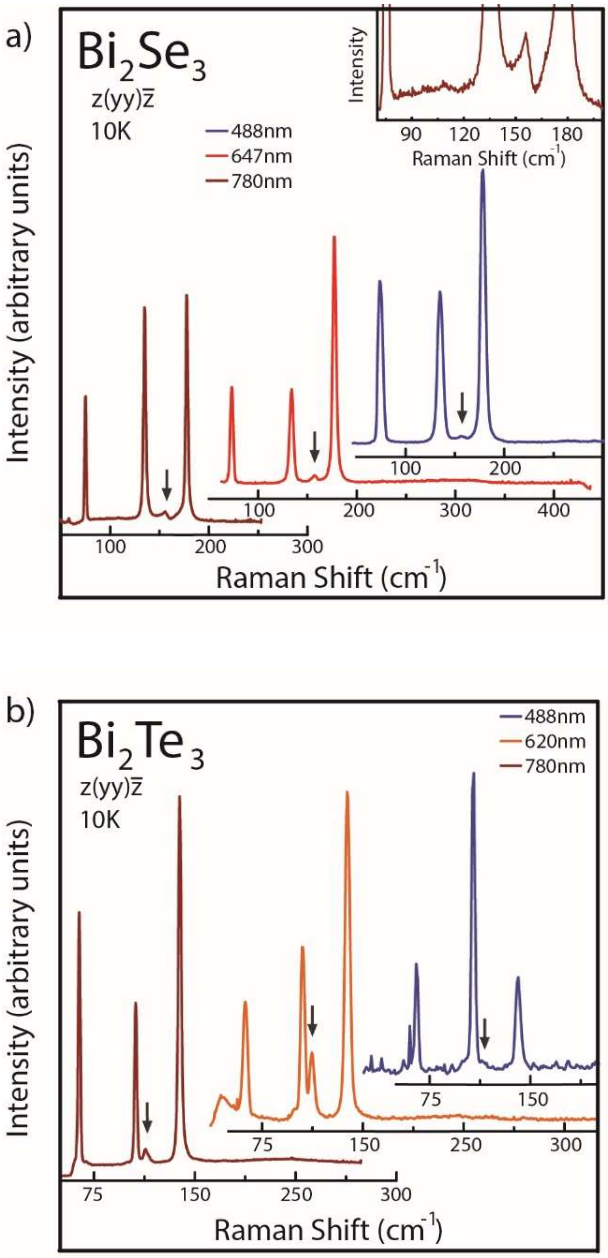

Figure 4.6: (a) Raman spectra of Bi_2Se_3 at various excitation wavelengths. The spectrum in the inset shows Fano-type interference. (b) Data for Bi_2Te_3. The intensity scale is linear in all cases.

As mentioned earlier, features which cannot be attributed to bulk vibrational modes have been previously reported in Raman studies of Bi_2Se_3 and Bi_2Te_3. Their origin remains controversial. Spectra of few-monolayer Bi_2Te_3 show lines at ~ 93 cm^{-1} and 114 cm^{-1} [11,14,15,16,17,18] and at ~ 160 cm^{-1} in Bi_2Se_3 [19,20], which were assigned to Raman-forbidden, infrared modes resulting from surface-induced symmetry breaking, while thin-film studies of Bi_2Te_3 reveal five additional peaks, one of which, at ~ 93 cm^{-1}, was assigned to a surface mode [21]. In bulk, single crystal of Bi_2Se_3, additional peaks at 68, 125, 129 and 160 cm^{-1} were observed and also assigned to Raman-forbidden polar modes [23]. Time-resolved photoemission data from single crystal Bi_2Se_3 shows an additional mode at 68.4 cm^{-1} [10], which was ascribed to a surface phonon strongly coupled to the surface electronic states. A detailed Raman study of thin films and single crystals of Bi_2Se_3 shows four additional modes that were assigned to surface phonons associated with particular bulk branches; their appearance was attributed to out-of-plane lattice distortions which are known to occur at the surface of the crystal [22].

The observation of extra Raman lines and, in particular, the lines we assign to surface phonons have been prevalently attributed in the literature to surface-induced symmetry breaking, which seemingly allows for scattering of nominally Raman forbidden, infrared-active modes [11,14,15,16,17,18,19,21,23]. For various reasons, we find such an interpretation to be incorrect. The frequencies of TO and LO phonons obtained from fits to infrared reflectivity spectra using a single-oscillator model [13] are listed in Table I. For Bi_2Te_3, we find that the position of the extra Raman line, at 114 cm^{-1}, is very close to that of the transverse component of the A_{1u}^2 mode. However, assigning the extra peak to such a TO mode would be inconsistent with the facts that (*i*) the width of this phonon is 6 cm^{-1} [13], which is approximately twice that of the Raman peak 3 cm^{-1}, and (*ii*) its direction of propagation is perpendicular to the scattering wavevector, which is

along [111]. To the best of our knowledge, experimental values of A_{1u} (infrared) phonon frequencies in Bi_2Se_3 are not available. Thus, one can only accurately state that the line we ascribe to a surface mode, at 159 cm^{-1}, does not match the values for E_u TO or LO modes. Nevertheless, given that the extra modes in Bi_2Se_3 and Bi_2Te_3 exhibit comparable behavior in regard to selection rules and λ_L dependence, we believe that the possibility that the Bi_2Se_3 Raman line at 159 cm^{-1} could be due to a TO or LO A_{1u} -mode is highly unlikely. Finally, we recall that the so-called "forbidden" LO-scattering, which relies on the Fröhlich interaction, is the only known mechanism by which a forbidden infrared mode can become Raman allowed [47], and that such a process displays a resonant enhancement that is stronger than that of allowed processes. Given the strong similarities between the two compounds, the fact that the extra peak in Bi_2Te_3 does not coincide in frequency with one of the LO modes strongly indicates that the additional lines in either compound cannot be ascribed to forbidden LO scattering. This is also supported by the observed weak λ_L-dependence of the intensity of the extra peaks, as noted previously.

Fig.4.7 shows phonon dispersion bands along the $\hat{c}$ axis of Bi_2Te_3 obtained by neutron scattering [48], and the frequency of the surface mode observed in our Raman data is indicated by the red dotted line. The fact that the frequency of this mode falls between two branches and does not intersect any of the phonon curves, is a strong indication of its surface origin. In other words, this mode does not propagate into the bulk and is truly a localized mode that exist only at the topmost layer. As of today, neutron data for Bi_2Se_3 is unavailable. Chapter V we will present resonant Raman data, which provides additional evidence of the surface nature of this mode in Bi_2Se_3.

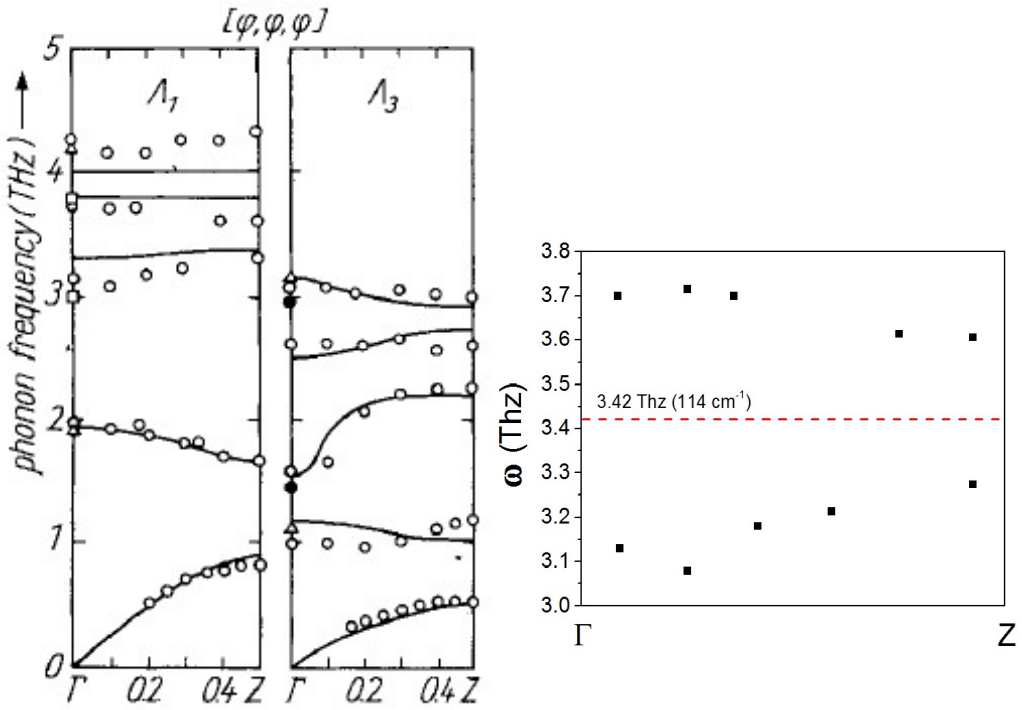

Figure 4.7: The phonon dispersion curves of Bi_2Te_3 along the trigonal axis [111] measured through neutron scattering at 77 K [48]. On the left, Λ_1 and Λ_2 indicate the longitudinal and transverse modes, respectively. The circles are experimental results and the solid lines are from calculations. The dots on the right plot are reproduced from the left plot and the dotted line is the frequency of the surface phonon we observe in our Raman measurements.

4. Density Functional Theory Calculations

This work was done by our collaborators Professor Emmanouil Kioupakis and Guangsha Shi from the Material Science Department at the University of Michigan. We present it here because it supports our assignment that the extra peaks we observe correspond to surface modes.

a) Methods

First-principles calculations of bulk and surface phonons of Bi_2Se_3 and Bi_2Te_3 were carried out using density functional theory [49], with norm-conserving pseudopotentials [50] and a plane-wave cutoff of 50 Ry, as implemented in the Quantum-Espresso code [51]. All calculations use the local-density approximation [52] for the exchange-correlation potential. We sampled the Brillouin zone using a shifted k-point grid of 10×10×10 for the bulk materials, and of 8×8×1 grid for the few-layer structures. The bulk and few-layer structures were relaxed with a convergence threshold of 10^{-6} Ry/a_0 for the forces on the atoms and 10^{-8} Ry for the total energy. Phonon frequencies and dynamical matrices were obtained using density-functional perturbation theory [53]. We included the non-analytic term to account for the splitting between the transverse-optical (TO) and longitudinal-optical (LO) modes at the Γ point of the Brillouin zone. For bulk materials, we used trigonometric polynomials to interpolate the phonon frequencies to 1000 points along the Γ–Z direction and subsequently calculated the density of states (DOS) corresponding to the Γ–Z modes using Gaussian functions and a broadening parameter of 0.2 cm^{-1}. Surface phonons of Bi_2Se_3 and Bi_2Te_3 were studied for 6-quintuple-layer slab structures.

b) Results and Discussion

The results of our first-principles calculations support our contention that the additional peaks we observe in Bi_2Se_3 and Bi_2Te_3 are due to surface phonons. Fig.4.8 shows the calculated frequencies and atomic displacements of surface phonons in both compounds from slab calculations, along with the Γ–Z bulk-phonon projected DOS. We see two surface modes (160.4 cm^{-1} and 183.2 cm^{-1} for Bi_2Se_3, and 117.5 cm^{-1} and 146.8 cm^{-1} for Bi_2Te_3). The calculated frequency of the low-frequency mode is in good agreement with experimental measurements in both compounds. The calculations show that these modes are strongly localized on the topmost quintuple layer of the slab structure, and that the calculated displacements, along the $\hat{c}$ axis, are in very good agreement with our experimental observation that the symmetry of these modes is A_{1g}. The fact that their frequencies fall in the gap regions of the corresponding bulk projected DOS and, thus, that they do not mix with bulk modes folded along the Γ–Z direction indicates that these modes are truly surface modes as opposed to surface resonances, which overlap in frequency with the bulk continuum. Our experimental data shows no clear evidence of the high frequency mode, which is expected to be in close proximity to and could be hidden underneath the strong, bulk A_{1g}^2 phonon.

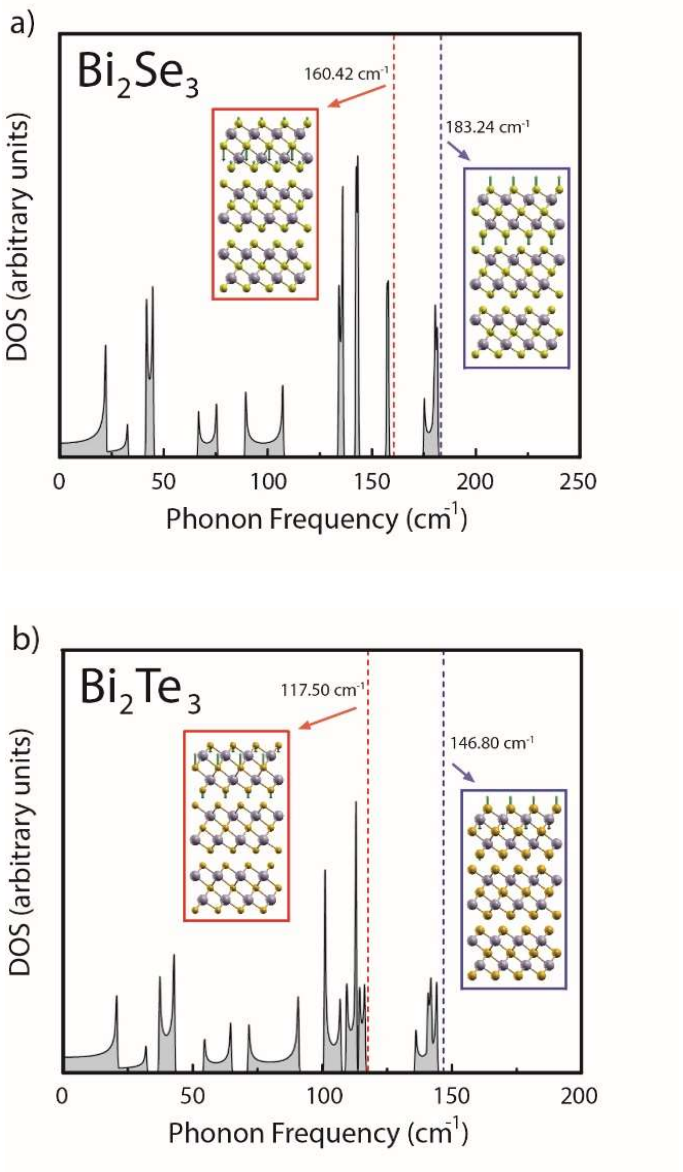

Figure 4.8: Calculated frequencies and corresponding atomic displacements for the two surface modes material from slab calculations: (a) 160.4 cm^{-1} and 183.2 cm^{-1} for Bi_2Se_3, and (b) 117.5 cm^{-1} and 146.8 cm^{-1} for Bi_2Te_3. The atomic displacements of the surface modes are localized primarily in the topmost quintuple layer. Calculated bulk phonon densities of states (DOS), projected along the Γ–Z direction, are also shown.

Spin-orbit interaction was not considered in the evaluation of the vibrational frequencies. Although spin-orbit coupling strongly affects the band structure of semiconductors with heavy elements such as Bi [54], and gives rise to the topologically insulating behavior [44], it is not important for the evaluation of structural properties or vibrational frequencies. The effect of spin-orbit coupling is secondary to the choice of the exchange-correlation function in affecting the accuracy of the calculated frequencies. For example, the zone-center phonon frequencies of Bi_2Se_3 and Bi_2Te_3 have been calculated [55] using the local density approximation (LDA) [56] and the Perdew-Burke-Exchange (PBE) [57] functionals. For both functionals, results were obtained both with and without spin-orbit coupling effects included in the calculation. The results show that the root mean square difference of the calculated frequencies determined with LDA upon inclusion of spin-orbit coupling (5.14 cm^{-1}) is smaller than the difference between the results obtained using the two different functionals (5.92 cm^{-1} when ignoring and 7.53 cm^{-1} when including spin-orbit coupling effects). In Table I, we list the bulk phonon frequencies from our theoretical and experimental work, as well as previously reported LDA calculations [44], which include spin-orbit coupling and infrared measurements [13] of phonon frequencies. The discrepancies between theory and experiment for the infrared modes may be attributed to the approximations involved in density functional theory (i.e.., the choice of the exchange-correlation functional and pseudopotentials) or due to higher-order effects such as phonon anharmonicity. We note that previous density functional theory calculations also show larger discrepancies with experiment for infrared modes [44].

5. Summary

In summary, we performed temperature- and excitation wavelength- dependent Raman scattering measurements in the topological insulators Bi_2Se_3 and Bi_2Te_3. In both compounds, and in addition to the features corresponding to the bulk Raman-allowed modes, our Raman measurements reveal a weak peak at low temperatures, which we assign to a surface phonon. First-principles calculations, which do not include spin-orbit coupling, reveal two modes localized at the topmost layers, one of which coincides in frequency with the extra peak and has a symmetry that is consistent with experimental results in both compounds.

References

[1] G. S. Nolas, J. Sharp, and H. J. Goldsmid, in Thermoelectrics: Basic Principles and New Materials Development (Springer, New York, 2001).

[2] M. Z. Hasan and C. L. Kane, Rev. Mod. Phys. 82, 30453067 (2010).

[3] D. Hsieh, Y. Xia, D. Qian, L. Wray, J. H. Dill, F. Meier, J. Osterwalder, L. Patthey, J. G. Checkelsky, N. P. Ong, A. V. Fedorov, H. Lin, A. Bansil, D. Grauer, Y.S. Hor, R. J. Cava, and M. Z. Hasan, Nature 460, 1101(2009).

[4] Y. Zhang, K. He, C.-Z. Chang, C.-L. Song, L.-L. Wang, X. Chen, J.-F. Jia, Z. Fang, X. Dai, W.-Y. Shan, S.-Q. Shen, Q. Niu, X.-L. Qi, S.-C. Zhang, X.-C. Ma, and Q.-K. Xue, Nat. Phys. 6, 584 (2010).

[5] Y. L. Chen, J. G. Analytis, J.-H. Chu, Z. K. Liu, S.-K. Mo, X. L. Qi, H. J. Zhang, D. H. Lu, X. Dai, Z. Fang, S. C. Zhang, I. R. Fisher, Z. Hussain, and Z.-X. Shen, Science 325, 178 (2009).

[6] V. Parente, A. Tagliacozzo, F. von Oppen, and F. Guinea, Phys. Rev. B 88, 075432 (2013).

[7] X. Zhu, L. Santos, R. Sankar, S. Chikara, C. Howard, F.C Chou, C. Chamon, and M. El-Batanouny, Phys. Rev. Lett. 107, 186102 (2011).

[8] C. Howard, M. El-Batanouny, R. Sankar, and F. C. Chou, Phys. Rev. B 88, 035402 (2013).

[9] Y. D. Glinka, S. Babakiray, and D. Lederman, J. Appl. Phys. 118, 135713 (2015).

[10] J. A. Sobota, S.-L. Yang, D. Leuenberger, A. F. Kemper, J. G. Analytis, I. R. Fisher, P. S. Kirchmann, T. P. Devereaux, and Z.-X. Shen, Phys. Rev. Lett. 113, 157401 (2014).

[11] K. M. F. Shahil, M. Z. Hossain, D. Teweldebrhan, and A. A. Balandin, Appl. Phys. Lett. 96, 153103 (2010).

[12] H. Köhler and C. R. Becker, Phys. Status Solidi B 61, 533 (1974).

[13] W. Richter and C. R. Becker, Phys. Status Solidi B 84, 619 (1977).

[14] L. Ren, X. Qi, Y. Liu, G. Hao, Z. Huang, X. Zou, L. Yang, J. Li, and J. Zhong, J. Mater. Chem. 22, 4921 (2012).

[15] R. He, Z. Wang, R. L. J. Qiu, C. Delaney, B. Beck, T. E. Kidd, C. C. Chancey, and X. P. A. Gao, Nanotechnology. 23, 455703 (2012).

[16] S. M. Souza, D. M. Trichês, C. M. Poffo, J. C. de Lima, T. A. Grandi, and R. S. de Biasi, J. Appl. Phys. 109, 013512 (2011).

[17] Y. Liang, W. Wang, B. Zeng, G. Zhang, Y. Song, X. Zhang, J. Huang, J. Li, and T. Li, Solid State Commun. 151, 704 (2011).

[18] V. Goyal, D. Teweldebrhan, and A. A. Balandin, Appl. Phys. Lett. 97, 133117 (2010).

[19] M. Eddrief, P. Atkinson, V. Etgens, and B. Jusserand, Nanotechnology 25, 245701 (2010).

[20] S. Y. F. Zhao, C. Beekman, L. J. Sandilands, J. E. J. Bashucky, D. Kwok, N. Lee, A. D. LaForge, S. W. Cheong, and K. S. Burch, Appl. Phys. Lett. 98, 14911 (2011).

[21] C. Wang, X. Zhu, L. Nilsson, J. Wen, G. Wang, X. Shan, Q. Zhang, S. Zhang, J. Jia, and Q. Xue, Nano Res. 6, 688 (2013).

[22] H. -H. Kung, M. Salehi, I. Boulares, A. F. Kemper, N. Koirala, M. Brahlek, P. Lošťák, C. Uher, R. Merlin, X. Wang, S.-W. Cheong, S. Oh, and G. Blumberg, Phys. Rev. B 95, 245406 (2017).

[23] V. Gnezdilov, Y. G. Pashkevich, H. Berger, E. Pomjakushina, K. Conder, and P. Lemmens, Phys. Rev. B 84, 195118 (2011).

[24] I. Boulares, G. Shi, E. Kioupakis, P. Lostak, C. Uher, and R. Merlin, Solid State Commun. 271, 1-5 (2011).

[25] P. Roushan, J. Seo, C. V. Parker, Y. S. Hor, D. Hsieh, D. Qian, A. Richardella, M. Z. Hasan, R. J. Cava, and A. Yazdani, Nature (London) 460, 1106 (2009).

[26] J. E. Moore, Nature 464, 194 (2010).

[27] A. Kitaey and C. Laumann, Lectures, Cornell University Library, 2009, http://arxiv.org/abs/0904.2771.

[28] D. Pesin and A. H. MacDonald, Nat. Mater. 11, 409 (2012).

[29] X. Zhang, J. Wang, and S. -C. Zhang, Phys. Rev. B 82, 245107 (2010).

[30] A. Soni, Z. Yanyuan, Y. Ligen, M. K. K. Aik, M. S. Dresselhaus, and Q. Xiong. Nano Lett. 12, 1203 (2012).

[31] F. Giorgianni, E. Chiadroni, A Rovere, M. Cestelli-Guidi, A. Perucchi, M. Bellaveglia, M. Castellano, D. D. Giovenale, G. D. Pirro, M. Ferrario, R. Pompili, C. Vaccarezza, F. Villa, A. Cianchi, A. Mostacci, M. Petrarca, M. Brahlek, N. Koirala, S. Oh, and S. Lupi, Nat. Commun. 7, 11421 (2016).

[32] A. Pertsova and C. M. Canali, New J. Phys. 16, 063022 (2014).

[33] Y. Zhao, X. Luo, J. Zhang, J. Wu, X. Bai, M. Wang, J. Jia, H. Peng, Z. Liu, S. Y. Quek, and Q. Xiong, Phys. Rev. B 90, 245428 (2014).

[34] Y. Kim, X. Chen, Z. Wang, J. Shi, I. Miotkowski, Y. P. Chen, P. A. Sharma, A. L. Lima Sharma, M. A. Hekmaty, Z. Jiang, and D. Smirnov, Appl. Phys. Lett. 100, 071907 (2012).

[35] Y. Yan, X. Zhou, H. Jin, C. Z. Li, X. Ke, G. V. Tendeloo, K. Lui, D. Yu, M. Dressel, and Z. M. Liao, ACS Nano 9, 10244 (2015).

[36] X. Zhang, Q. H. Tan, J. B. Wu, W. Shi, and P. H. Tan, Nanoscale 8, 6435 (2016).

[37] V. Wagner, G. Dolling, B. M. Powell, and G. Landwehr, Phys. Status Solidi B 85, 311 (1978).

[38] A. D. LaForge, A. Frenzel, B. C. Pursley, T. Lin, X. Liu, J. Shi, and D. N. Basov, Phys. Rev. B 81, 125120 (2010).

[39] M. Bianchi, D. Guan, S. Bao, J. Mi, B. B. Iversen, P. D.C. King, and P. Hofmann, Nat. Commun. 1, 128 (2010).

[40] F.-T. Huang, M.-W. Chu, H. H. Kung, W. L. Lee, R. Sankar, S. –C. Liou, K. K. Wu, Y. K. Kuo, and F. C. Chou, Phys. Rev. B 86, 081104 (2012).

[41] C. B. Satterthwaite and R. W. Ure, Jr., Phys. Rev. 108, 1164 (1957).

[42] E. Lahoud, E. Maniv, M. Shaviv Petrushevsky, M. Naamneh, A. Ribak, S. Wiedmann, L. Petaccia, Z. Salman, K. B. Chashka, Y. Dagan, and A. Kanigel, Phys. Rev. B 88, 195107 (2013).

[43] Y. Yan, X. Zhou, H. Jin, C. Z. Li, X. Ke, G. V. Tendeloo, K. Lui, D. Yu, M. Dressel, and Z. M. Liao, ACS Nano 9, 10244 (2015).

[44] O. V. Yazyev, E. Kioupakis, J. E. Moore, and S. G. Louie, Phys. Rev. B 85, 161101 (2012).

[45] R. Merlin, A. Pinczuk and W. H. Weber, in Raman Scattering in Materials Science, ed. by W. H. Weber and R. Merlin (Springer, Berlin, 2000), p. 12.

[46] U. Fano, Phys. Rev. 124, 6 (1961).

[47] M. Cardona, in Topics in Applied Physics: Light Scattering in Solids II (Springer, Berlin, 1982), Vol. 50, p. 128.

[48] W. Kullmann, G. Eichhorn, H. Rauh, R. Geick, G. Eckold, and U. Steigenberger, Phys. Stat. sol. (b) **162**, 125 (1990).

[49] W. Kohn and L. J. Sham, Phys. Rev. 140, A1133 (1965).

[50] N. Troullier and J. L. Martins, Phys. Rev. B 43, 1993 (1991).

[51] P. Giannozzi et al., J. Phys. Condens. Matter 21, 395502 (2009).

[52] P. Perdew and A. Zunger. Phys. Rev. B 23, 5048 (1981).

[53] S. Baroni, S. de Gironcoli, A. Dal Corso, and P. Giannozzi, Rev. Mod. Phys. 73, 515 (2001).

[54] E. Kioupakis, M. L. Tiago, and S. G. Louie, Phys. Rev. B 82, 245203 (2010).

[55] X. Luo, M. B. Sullivan, and S. Y. Quek, Phys. Rev. B 86, 184111 (2012).

[56] D. M. Ceperley and B. J. Alder, Phys. Rev. Lett. 45, 566 (1980).

[57] J. Perdew, K. Burke, and M. Ernzerhof, Phys. Rev. Lett. 77, 3865 (1996).

CHAPTER V

Resonant Raman Scattering in the Topological Insulator Bi_2Se_3

In this chapter, we present experimental results of low-temperature resonant Raman scattering in bulk Bi_2Se_3, which support our assignment of the surface origin of the extra peak. This mode was discussed in chapter IV and was suggested by local density approximation calculations that it is localized at the surface. Here, we provide additional experimental evidence supporting such assignment. We first discuss the cross-section dependence of *A*-type bulk phonons on the excitation energy. We then show that the surface mode exhibits an asymmetric-Fano-profile when the excitation energy is near-resonance with a surface exciton. Prior to addressing our results, we give a brief description of the surface electronic band structure of Bi_2Se_3, as it is important in interpreting our data.

1. Surface Band Structure of Bi_2Se_3

When the energies of the incident and/or scattered light are close to an interband gap or an exciton of the scattering medium, the coupling of light to optical transitions is enhanced. Therefore, a knowledge of a material's band structure provides essential information to interpret resonant Raman scattering data. As mentioned before, the surface electronic states in Bi_2Se_3 are gapless and are characterized by a linear dispersion known as Dirac states. ARPES measurements identify two

Dirac cones, consistent of occupied (SS1) and unoccupied (SS2) surface states, which are separated by an energy gap of 1.8 eV [1]. Fig.5.1 shows the surface band structure of Bi_2Se_3 obtained by Sobota *et al*. through ARPES (on the left) as well as slab band calculations (on the right) [2]. It is clear from Fig.5.1 that the second linearly dispersing surface state is unoccupied and 1.8 eV above SS1. The existence of such interband transition at the surface provides a way to distinguish optical transitions, example: collective excitations, whose scattering processes involve the surface from those of the bulk.

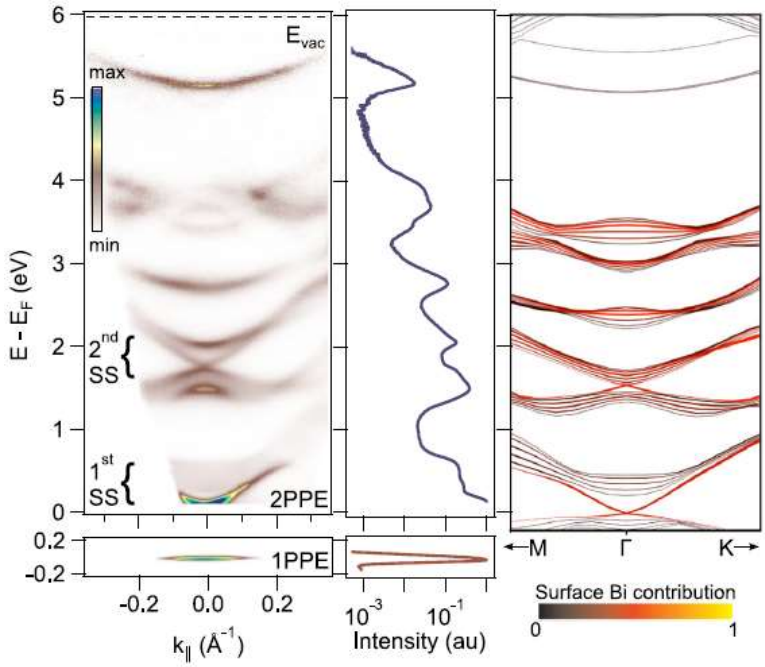

Figure 5.1: a) Surface electron dispersion curves of Bi_2Se_3 obtained by ARPES. Results obtained by one- and two-photoemission (1PPE and 2PPE) are in the lower and top boxes, respectively. SS1 and SS2 refer to the occupied and unoccupied Dirac states, respectively. b) Shows momentum-integrated energy distribution curves. c) Band calculations of the surface states in Bi_2Se_3. Results were obtained by Sobota *et al*. [1].

A previous Raman work on Bi_2Se_3 reported a peak at 150 meV, which was identified as the transverse collective spin mode of surface Dirac fermions [3]. Fig.5.2 shows the Raman spectra at various excitation energies obtained by Kung *et al*. [3]. The peak appears only in the antisymmetric A_2 scattering representation, a representation whose basis functions transform as the *z* component of the angular momentum. This is consistent with their assignment that the peak corresponds to a spin mode which carries a magnetic moment perpendicular to the surface. The topological nature of the spin mode is evident when the energy of the incoming light (1.83 eV) is near-resonance with the transition between SS1 and SS2 (1.8 eV) as the peak's strength significantly increases. Kung *el al*. performed Raman cross-section calculations of spin-flip processes, between the SS1 and SS2 states, under resonance and found very good agreement with experimental observations (for more details, see reference [3]).

The spectra in Fig.5.2 also shows a photoluminescence line at 1.54 eV. Such emission line was attributed to a surface exciton due to the fact that its emission has a threshold of about 1.8 eV, the energy difference between the two surface Dirac points (see right plot in Fig.5.2). This assignment is consistent with the resonant behavior the surface spin mode exhibits. The peak corresponding to the surface spin mode is absent in the 521 nm (2.38 eV) spectrum as it is farthest from surface interband transitions. However, as the excitation energy nears the SS1-SS2 gap in the 647 nm (1.92 eV) spectrum, the peak shows a weak presence. When the excitation energy is near-resonance with the exciton (1.54 eV), in the 752 nm (1.65 eV) spectrum, the signal increases. In the 676 nm (1.83 eV) spectrum, the peak is strongest as the incident and scattered light are in near-resonance with the SS1-SS2 transitions and the surface exciton, respectively.

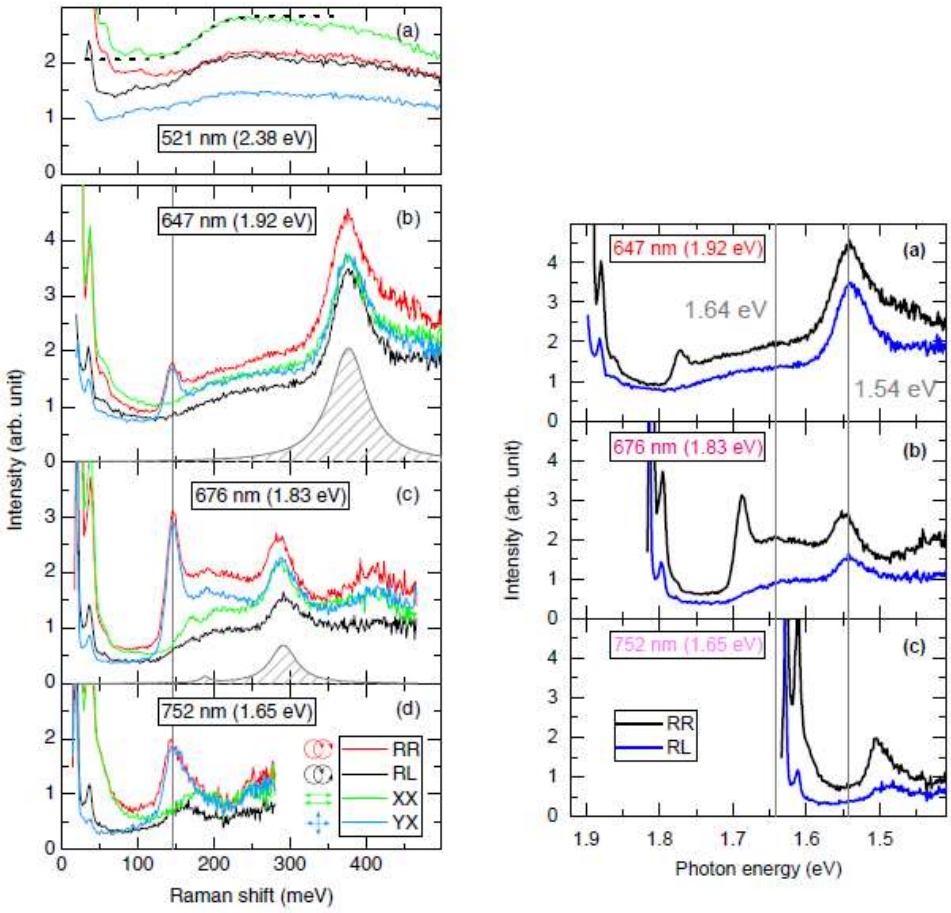

Figure 5.2: Raman scattering spectra showing a chiral spin mode and a surface exciton emission line with respect to the Raman shift (left graph) and photon energy (right graph). Note the resonance in (b) and (d) occur when in energy of the incoming light is in near resonance with the SS1-SS2 transitions (1.8 eV) and the exciton line (1.54 eV), respectively. (c) Shows a possible double-resonance as the energy of the incoming and outgoing light are close to the SS1-SS2 transitions and exciton emission line, respectively. Results were obtained by Kung *el al*. [3].

2. Experimental Methods

Raman spectra were acquired at 10 K in the backscattering geometry with the scattering wavevector along the $\hat{c}$ axis of Bi_2Se_3 single crystal. Measurements were carried out with several lines of argon-ion, rhodamine-dye and Ti:sapphire cw lasers. The incident laser power used ranged from 20 to 25 mW. We checked the scattering intensity of surface and bulk phonons as a function of power, and found that up to 30 mW, the intensity scales linearly for all phonons - this insures that heating and space-charge electric fields due to electron-hole pairs from absorption are negligible. We use the same Dilor XY spectrometer.

Optical constants measured through ellipsometry at room temperature were used in obtaining resonance curves. They were also determined at 10 K for several wavelengths through Fresnel reflection measurements, and the variation from their room temperature values were found to be insignificant (this is discussed thoroughly in chapter III).

3. Results and Discussion

Prior to discussing our results regarding the surface mode, we present data showing the resonant behavior of the A_{1g} bulk modes. Fig.5.3 shows resonance curves - the intensity of the scattering by phonons as a function of the excitation energy ω_L - for the scattering by bulk A_{1g}^1 and A_{1g}^2 modes, as well as a theoretical curve of fully symmetric A-type phonons under resonance (see Eq.2.36) [4]. Note that in obtaining the experimental data, we corrected for absorption and reflection losses, as detailed in chapter III. The assumptions made in deriving the theoretical expression for the Raman cross-section of A-like phonons ($\sigma(A) \propto \left|\frac{d\chi}{d\omega_L}\right|^2 \omega_L^4$) are as follows: (1) the deformation-potential is constant, (2) phonon-induced interband transitions (referred to as

three-band processes in chapter II) are insignificant, and (4) the electronic wavefunctions are unchanged by the atomic displacements of the ions.

The Raman intensity of the A_{1g} bulk modes closely follows the theoretical prediction in the range 1.4 – 2.8 eV indicating a broad resonance. In addition, we may conclude that over this frequency region, the deformation-potential for both A_{1g} modes, to a good approximation, is constant. Therefore, the scattering by A_{1g} phonons is determined mainly by the combined density of electronic states. This conclusion can be achieved since $\partial\chi/\partial\omega_L$ is the term, in addition to the factor ω_L^4, which brings about the dependence of the cross-section on ω_L (see Eq.2.36). The electric susceptibility for interband transitions can be written in the form [4]

$$\chi = B\left|< 0\left|p_\mu(\boldsymbol{k}_2)\right|\beta >\right|^2 f(\hbar\omega_L, E_g)$$

where B is a constant, $< 0\left|p_\mu(\boldsymbol{k}_2)\right|\beta >$ is the momentum matrix element of the interband transitions and $f(\hbar\omega_L, E_g)$ is related to the combined density of electronic states – E_g denotes the energy difference between the bands at ω_L. Recall that in deriving Eq.2.36, we made the assumption that *A*-like phonons mostly affect energy bands involved in the scattering process and not their corresponding wavefunctions. This is a reasonable assumption for phonons with diagonal Raman tensors since they preserve the symmetry of the crystal structure during the oscillations. Hence, $< 0\left|p_\mu(\boldsymbol{k}_2)\right|\beta > \approx$ constant and $f(\hbar\omega_L, E_g)$ is the main contributor to the change in the electric susceptibility with respect to the excitation wavelength.

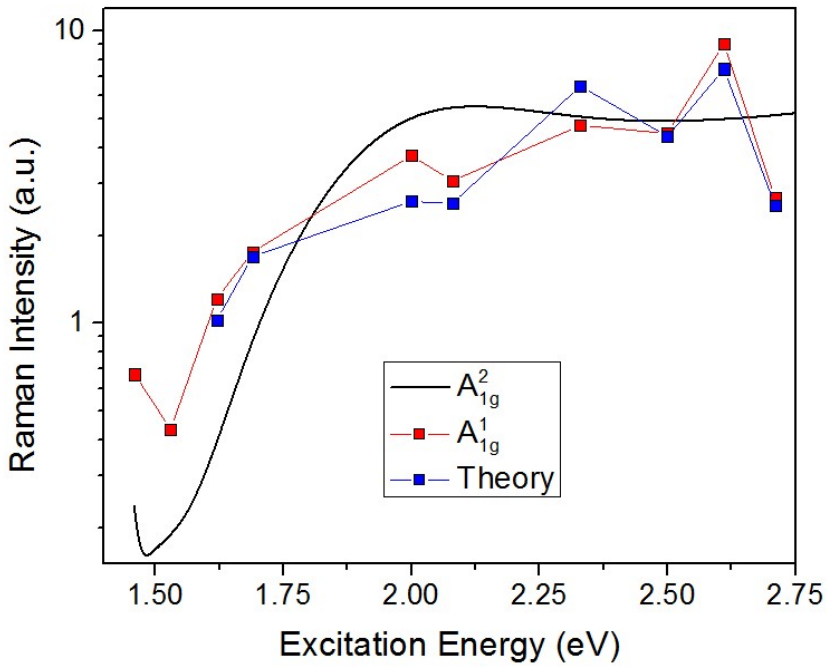

Figure 5.3: Resonance curves for the scattering by A_{1g}^1 and A_{1g}^2 bulk modes (dots) and theoretical results of A-type symmetry bulk phonons calculated from the expression $\left|\frac{d\chi}{d\omega_L}\right|^2 \omega_L^4$, where the electric susceptibility χ was measured by means of ellipsometry.

Fig.5.4. shows the ratio of the Raman cross-section of the surface phonon to bulk A_{1g}^2 mode with respect to the excitation energy. Although the surface mode is of A symmetry (see chapter IV), it displays a different resonant behavior in comparison to the A_{1g} bulk modes, particularly as ω_L decreases. As explained below, this is consistent with our assignment that this mode is of surface origin. As the data strongly suggests, the scattering of such mode involves electronic bands whose origin is the surface.

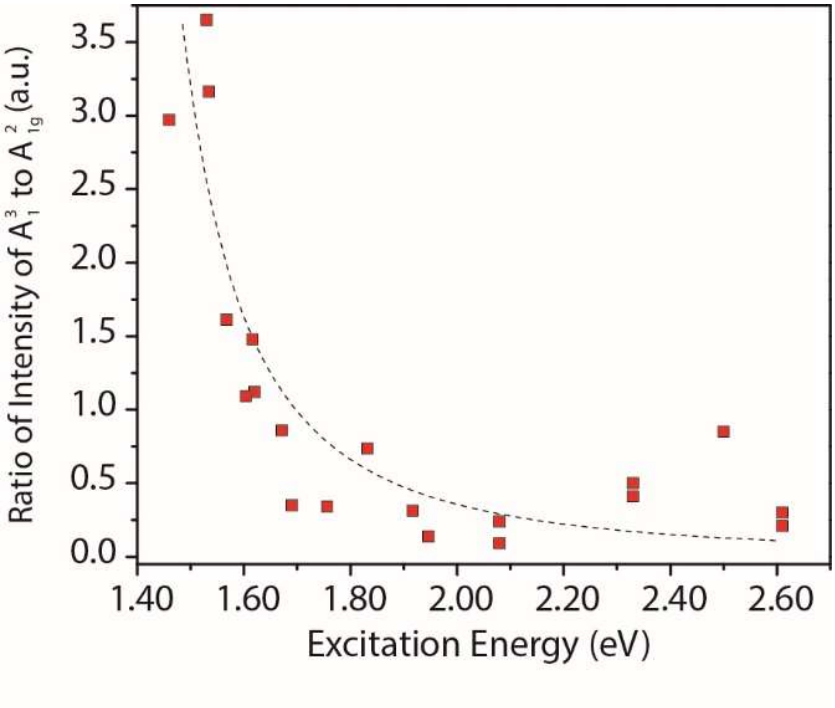

Figure 5.4: Ratio of the Raman cross-section of the surface phonon (referred to as A_1^3) to bulk's A_{1g}^2 in Bi_2Se_3.

In resonant scattering and under the quasi-static approximation (phonon frequency << ω_L), the first-order modulated susceptibility in Eq.2.36 reduces to

$$\delta\chi_{\mu\nu} \propto \sum_{\alpha\beta}\{\frac{<0|p_\mu(\boldsymbol{k}_2)|\beta>\cdot<\beta,\bar{n}\pm1|H_{EL}|\alpha,\bar{n}>\cdot<\alpha|p_\nu(-\boldsymbol{k}_1)|0>}{(E_\beta-\hbar\omega_L)(E_\alpha-\hbar\omega_L)}\}.$$

It is obvious that the terms which control $\delta\chi$, and hence the cross-section, are in the denominators as they vanish when the excitation energy nears electronic transitions. Since the scattering of phonons with the same symmetry and origin involve the same intermediate transitions (E_β and E_α), their corresponding cross-section curves under resonance show similar behavior. This is clearly seen in Fig.5.3 with the A_{1g}^1 and A_{1g}^2 modes. The fact that the surface mode, although of *A*

symmetry, shows a different behavior than the A bulk modes, is suggestive that the phonon is of a different origin. Moreover, the intensity of the surface mode in comparison to the A_{1g}^2 mode significantly increases as ω_L approaches the energy of the surface exciton (1.54 eV), indicating that the intermediate transitions involve the surface exciton – addition evidence of the surface nature of the extra peak.

Fig. 5.5 shows Raman spectra of the surface mode in the $z(yy)\bar{z}$ scattering geometry at different excitation energies. The spectra are centered about the position of the peak in the 2.54 eV spectrum (Ω). The data shows a clear dependence of the peak's shape and position on excitation energy. The peak's lineshape is symmetric in the 2.54 and 2.41 eV spectra. However, as ω_L approaches ≈ 1.65 eV, the lineshape become asymmetric. This occurs due an increase in the cross-section on the left slope of the profile and a decrease on the right which results in a shift in the peak's position – note the dip on the left side of the profile. Such behavior is a clear indication that an interference is at work. We characterize such interference as a Fano-resonance – details are discussed below. From a first glance, one can suspect such behavior from noting that the shift in the peak's position is larger as the asymmetry is more pronounced - a characteristic of Fano-interference.

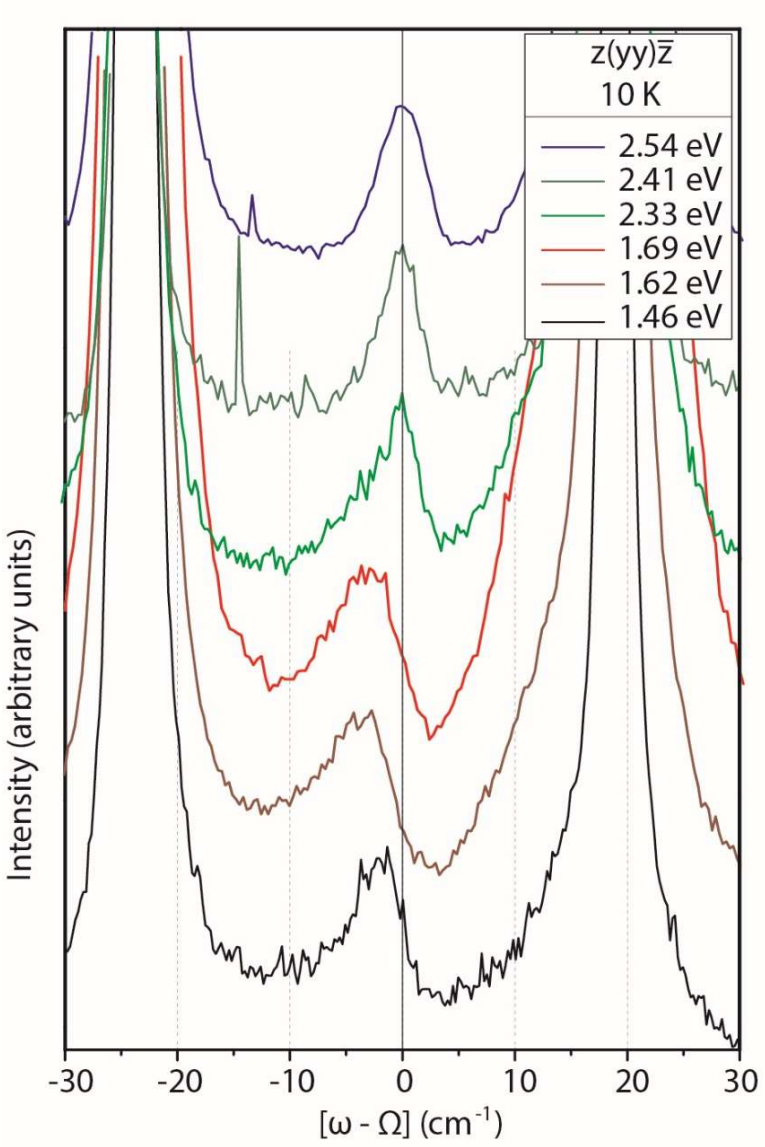

Figure 5.5: Raman spectra of the surface phonon at Ω = 159 cm^{-1} in Bi_2Se_3 at various excitation energies. The spectra were acquired in the $z(yy)\bar{z}$ configuration and at 10 K temperature. They are shifted vertically with respect to each other and centered about Ω.

As mentioned in chapter II, Fano-resonances produce an asymmetric spectral profile due to the interference of two scattering amplitudes associated with a discrete state and a continuum to which the discrete state is coupled. The discrete state and the coupled continuum must overlap in energy and have the same symmetry. The resulting asymmetry in the spectral profile is measured by the quantity q, named the asymmetry parameter. This parameter relates to Raman scattering amplitudes of the interacting states as $q \propto \frac{R_{ph}}{R_e}$, where R_{ph} and R_e are the amplitudes of the discrete state and the coupled continuum, respectively (see chapter II for more details on Fano-interference). We obtain values of q, as a function of ω_L, via lineshape fits as well as from the shifts in the peak position. Profiles of the surface mode in all spectra can be fitted with the same spectral width value of $\Gamma = 4.1$ cm^{-1} – this is consistent with the fact that Γ^{-1} is proportional to the lifetime of the phonon which is independent of ω_L. As for the values of q obtained through the shift in the position, we use the equation $\delta\Omega = \Gamma/q$ from Fano theory, with $\Gamma = 4.1$ cm^{-1}. The quality of the fits (see inset in Fig.5.4) and the consistency of both results from lineshape fits and position shifts are very good and support our contention that such interference is indeed of the Fano-type.

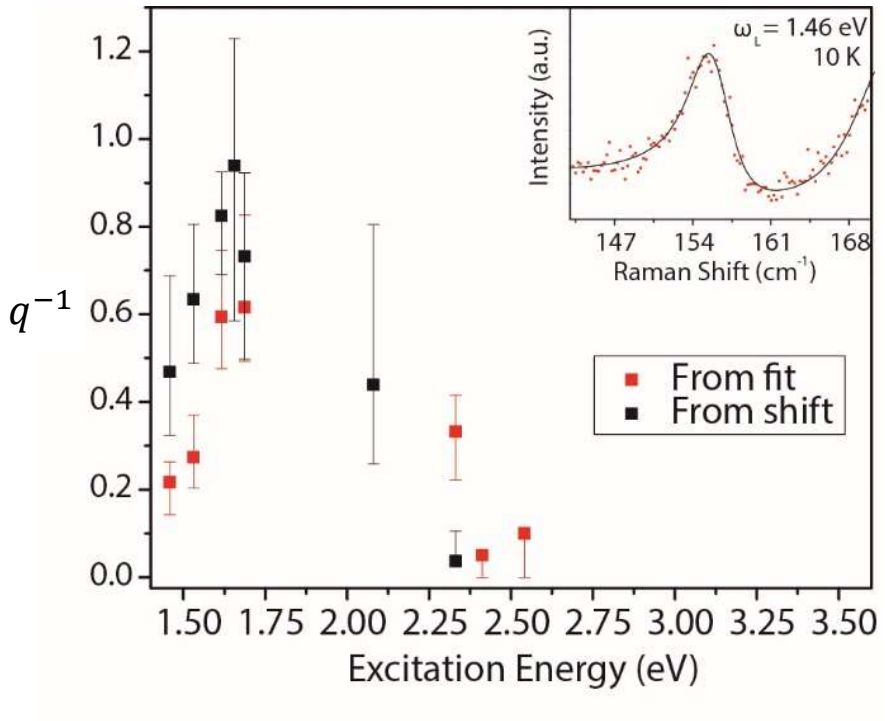

Figure 5.6: Plot of q^{-1} vs excitation energy as obtained from line shape fits (red) and position shifts of the peak (blue) of the surface phonon (159 cm^{-1}) in Bi_2Se_3. The inset shows the surface phonon line shape, 1.46 eV excitation energy, and its fit as obtained by the Fano expression.

Fig.5.6, we show a plot of $1/q$ with respect to ω_L. Note the consistency of the data obtained from the fits and shifts in the peak position. Both exhibit identical behavior and are consistent in showing a peak at $\omega_{L(\max)} \approx 1.65$ eV. The most interesting piece in Fig.5.6 is that the energy in which $1/q$ is maximum ($\omega_{L(max)}$) is close to that of the previously reported surface exciton (1.54 eV) [3]. This is a strong indication that the scattering mechanism of the phonon and the coupled continuum involves the intermediate excitation of such electron-hole pair state, and hence a confirmation of their surface origin.

Although q has a ω_L dependence, which denotes that the scattering by the phonon and the coupled continuum have a different dependence on ω_L, we expect both R_{ph} and R_e to resonate since they involve the same intermediate electronic bands in their scattering process. This is consistent with the observed relative increase of the surface mode's cross-section ($\sigma \propto \left|R_{ph}\right|^2$) near the energy of the surface exciton (1.54 eV) in Fig.5.4. The resonance in the cross-section of the coupled continuum $\propto \left|\left(\frac{1}{q}\right) \cdot R_{ph}\right|^2$ is obvious as $1/q$ displays a peak in at 1.65 eV. Note that the small discrepancies in $\omega_{L(max)}$ and the energy of the exciton line is most likely due the different ω_L dependence of the phonon and continuum's scattering amplitudes as they have two and one resonant denominators, respectively [5].

The conclusion we obtain from the experimental data presented thus far, namely the facts that (1) the surface phonon's scattering process is different than bulk phonons of the same symmetry and (2) the surface phonon's coupling to a continuum to which shows a clear resonant behavior with a surface exciton line, confirm the surface origin of the phonon at $\Omega = 159$ cm^{-1}. These results are consistent with local density approximation calculations presented in chapter VI in that they reveal an *A*-type symmetry localized surface mode at $\Omega = 160$ cm^{-1}. Our results are also consistent with previous ARPES measurements in Bi_2Se_3, which reported strong electron-phonon coupling revealed in the form of a "kink" in the topological surface states' energy bands at ~ 20 meV (160 cm^{-1}) [6,7].This reaffirms our results and indicates that the continuum to which the surface phonon is coupled is due to electronic transitions involving Dirac surface states.

4. Summary

In summary, we showed evidence of the surface nature of the extra peak observed at 159 cm^{-1} in Bi_2Se_3 Raman spectra. This mode displays a different resonant behavior in comparison to bulk modes and, most importantly, a Fano-resonance which becomes more pronounced as the excitation frequency nears that of a surface exciton. Our assignment that the mode is a surface phonon and the coupled continuum is due to electronic transitions involving Dirac states is consistent with (1) previous ARPES measurements [6,7], which show strong electron-phonon coupling in the topological surface states at a frequency that coincide with the extra line, and (2) LDA calculations which reveals a surface phonon of A-symmetry and frequency 159 cm^{-1}.

References

[1] D. Niesner, Th. Fauster, S. V. Eremeev, T. V. Menshchikova, Yu. M. Koroteev, A. P. Protogenov, E. V. Chulkov, O. E. Tereshchenko, K. A. Kokh, O. Alekperov, A. Nadjfov, and N. Mamedov, Phys. Rev. B 86, 205403 (2012).

[2] J. A. Sobota, S.-L. Yang, A. F. Kemper, J. J. Lee, F. T. Schmitt, W. Li, R. G. Moore, J. G. Analytis,

I. R. Fisher, P. S. Kirchmann, T. P. Devereaux, and Z.-X. Shen1,2,3, Phys. Rev. Lett. 111, 136802 (2013).

[3] H.-H. Kung, S. Maiti, X. Wang, S.-W. Cheong, D. L. Maslov and G. Blumberg, Phys. Rev. Lett. 119, 136802 (2017).

[4] W. Richter, in Springer Tracts in Modern Physics: Resonant Raman Scattering in Semiconductors (Springer, New York, 1976), Vol 78, p. 121.

[5] M. Cardona, Topics in Applied Physics: Light Scattering in Solids I (Springer-Verlag Berlin Heidelberg, 1983).

[6] C. Chen, Z. Xie, Y. Feng, H. Yi, A. Liang, S. He, D. Mou, J. He, Y. Peng, X. Liu, Y. Liu, L. Zhao, G. Liu, X. Dong, J. Zhang, L. Yu, X. Wang, Q. Peng, Z. Wang, S. Zhang, F. Yang, C. Chen, Z. Xu, and X. J. Zhou, Sci. Rep. **3**, 2411 (2013).

[7] T. Kondo, Y. Nakashima, Y. Ota, Y. Ishida, W. Malaeb, K. Okazaki, S. Shin, M. Kriener, S. Sasaki, K. Segawa, and Y. Ando, Phys. Rev. Lett. 110, 217601 (2013).

CHAPTER VI

Conclusions

Bi_2Se_3 and Bi_2Te_3 have been at the center of an intense pursuit to fully understand the surface electronic properties of topological insulators. Through Raman scattering measurements and first principles LDA calculations, this dissertation investigated surface atomic vibrations and their relevance to the topological surface states in Bi_2Se_3 and Bi_2Te_3. Experimental results show the existence of *localized* surface phonons in both compounds. Calculations support the experimental findings and suggest that the existence of these surface modes is unrelated to the topological surface states. Experiments also show that the surface phonon in Bi_2Se_3 (at 159 cm^{-1}) couples to an electronic continuum, which involves Dirac surface states. Moreover, results presented in chapter V demonstrate that Raman scattering provides an efficient way to probe surface excitations in topological insulators - a new and convenient means to discriminate surface excitations from bulk modes.

Although our findings provide significant insight into the surface vibrations in Bi_2Se_3 and Bi_2Te_3, much work remains to be done to fully understand the topological properties of these compounds. While the surface electronic states of Bi_2Se_3 are very well characterized, little to no experimental work characterizing optical interband transitions at the surface of Bi_2Te_3 exist. This is an area where Raman scattering may contribute. Chapter V studies the cross-section of phonon modes in

Bi_2Se_3 with respect to the excitation frequency. One of the findings was that the ratio of the surface phonon intensity to that of the A_{1g}^2 mode shows a resonance at the frequency of a known surface exciton. The same approach may be carried out in Bi_2Te_3 to identify interband transitions or excitons at the surface. Caution with the incident beam's power and time of exposure of the sample to the beam must be taken into account, however. It is well known that in tellurium-based chalcogenides, laser exposure induces decomposition leading to tellurium segregation at the interface [1]. One of the phonon modes in tellurium carries the same frequency and symmetry as the surface phonon in Bi_2Te_3 discussed in this work. To avoid these effects, in my experience, it is necessary to cleave the sample prior to measurements, maintain the beam power below 3 mW and occasionally change the beam spot on the sample. Moreover, although not related to the topological surface states, studying the effects of laser exposure in terms of power and time to induce decomposition in Bi_2Te_3 is another avenue of research that can be explored.

Future directions of this research may also include examining the decay mechanism of the surface phonon in Bi_2Se_3 as it may provide more insight into the robustness of the topological surface states. These studies can be carried out through temperature-dependent Raman measurements on samples of different carrier concentration. Preliminary data from our temperature-dependent experiments show that the decay process of the surface mode in Bi_2Se_3 is different than its counterpart in Bi_2Te_3 – this is consistent with the interpretation that the surface phonon in Bi_2Se_3 is coupled to an electronic continuum. Fig.6.1 displays the ratio of the cross-section of the surface phonon to bulk modes in both compounds with respect to temperature. Unlike, the surface phonon in Bi_2Te_3, which displays a similar behavior as the bulk modes, the surface mode in Bi_2Se_3 shows a stronger decay in comparison to bulk modes as temperature is increased. Hence, by performing the same measurements on samples of different carrier concentration, it may be possible to obtain

a measure of the decay of the surface phonon that is due to the coupling to the electronic continuum. Furthermore, the study the Fano-resonance of the surface phonon in Bi_2Se_3 in samples of varying carrier concentration may yield interesting results.

Since their theoretical discovery, topological insulators remain one of the hottest topics in solid state physics. Their novel and exotic properties make them, not only attractive from a fundamental point of view, but their potential applications opened new possibilities. Although much work remains, our understanding of their surface states has significantly advanced. It certainly has been an exciting journey to be a part of these developments.

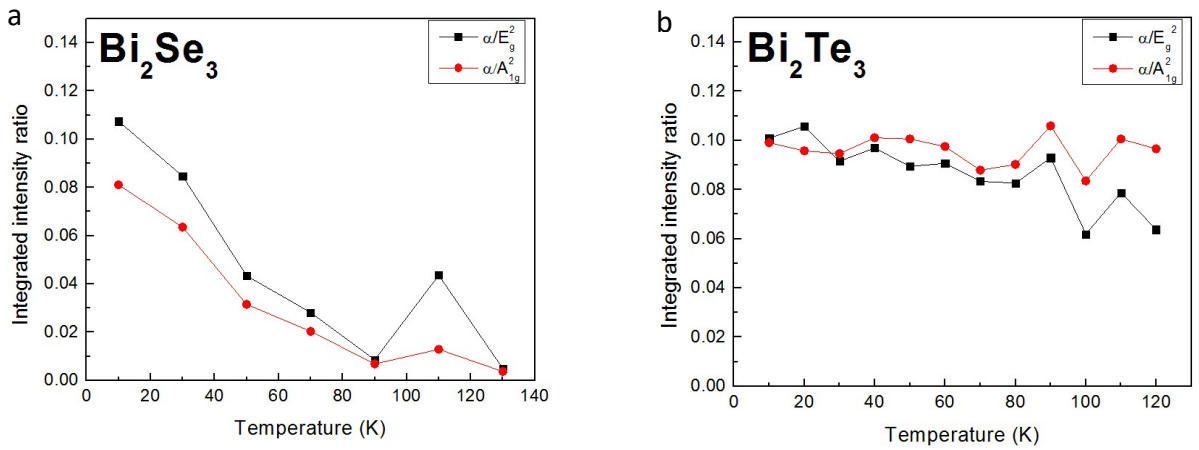

Figure 6.1: Ratio of integrated intensity of surface phonon (referred to as α) to bulk modes E_g^2 and A_{1g}^2 as a function of temperature

References

[1] Y. Li, V. A. Stoica, L. Endicott, G. Wang, C. Uher, and R. Clarke, Appl. Phys. Lett. 97, 171908 (2010).